Monthly Notices of the ROYAL ASTRONOMICAL SOCIETY
MNRAS **441,** 3417–3443 (2014) doi:10.1093/mnras/stu636

Massive compact galaxies with high-velocity outflows: morphological analysis and constraints on AGN activity

P. H. Sell,[1,2★] C. A. Tremonti,[1] R. C. Hickox,[3] A. M. Diamond-Stanic,[1] J. Moustakas,[4] A. Coil,[5] A. Williams,[1] G. Rudnick,[6] A. Robaina,[7] J. E. Geach,[8] S. Heinz[1] and E. M. Wilcots[1]

[1]*Department of Astronomy, University of Wisconsin-Madison, Madison, WI 53706-1582, USA*
[2]*Department of Physics, Texas Tech University, Lubbock, TX 79409-1051, USA*
[3]*Department of Physics and Astronomy, Dartmouth College, Hanover, NH 03755-3528, USA*
[4]*Department of Physics and Astronomy, Siena College, 515 Loudon Road, Loudonville, NY 12211-1462, USA*
[5]*Center for Astrophysics and Space Sciences, University of California, San Diego, La Jolla, CA 92093-0424, USA*
[6]*Department of Physics and Astronomy, 1251 Wescoe Hall Drive, University of Kansas, Lawrence, KS 48109-1042, USA*
[7]*Department of Astronomy, University of Michigan, 550 Church Street, Ann Arbor, MI 66045-7582, USA*
[8]*Centre for Astrophysics Research, University of Hertfordshire, Hatfield, Hertfordshire AL10 9AB, UK*

Accepted 2014 March 31. Received 2014 March 19; in original form 2014 January 20

ABSTRACT

We investigate the process of rapid star formation quenching in a sample of 12 massive galaxies at intermediate redshift ($z \sim 0.6$) that host high-velocity ionized gas outflows ($v > 1000$ km s^{-1}). We conclude that these fast outflows are most likely driven by feedback from star formation rather than active galactic nuclei (AGNs). We use multiwavelength survey and targeted observations of the galaxies to assess their star formation, AGN activity, and morphology. Common attributes include diffuse tidal features indicative of recent mergers accompanied by bright, unresolved cores with effective radii less than a few hundred parsecs. The galaxies are extraordinarily compact for their stellar mass, even when compared with galaxies at $z \sim 2$–3. For 9/12 galaxies, we rule out an AGN contribution to the nuclear light and hypothesize that the unresolved core comes from a compact central starburst triggered by the dissipative collapse of very gas-rich progenitor merging discs. We find evidence of AGN activity in half the sample but we argue that it accounts for only a small fraction ($\lesssim$10 per cent) of the total bolometric luminosity. We find no correlation between AGN activity and outflow velocity and we conclude that the fast outflows in our galaxies are not powered by ongoing AGN activity, but rather by recent, extremely compact starbursts.

Key words: galaxies: active – galaxies: evolution – galaxies: interactions – galaxies: starburst.

1 INTRODUCTION

Cosmological simulations based on a lambda cold dark matter framework overpredict by an order of magnitude the fraction of baryons that will form stars by the present day (e.g. Kereš et al. 2009). This ‘overcooling’ problem is manifested at the massive end ($M_* \sim 10^{11}$ M$_\odot$) by simulated galaxies that are too luminous and blue to match observations (e.g. Croton et al. 2006; Gabor et al. 2011). The preferred solution is that feedback from massive stars and accreting supermassive black holes (SMBHs) regulates the cold gas supply for star formation by ejecting cold gas from galaxies and preventing hot gas from cooling.

The global effect of this feedback can be tuned to match the observed stellar mass function by reducing the efficiency of star formation in both low-mass and high-mass dark matter haloes (e.g. Somerville 2009; Behroozi, Wechsler & Conroy 2013). However, the relevant gas physics (e.g. shocks, dissipation, heating, cooling) occurs on scales that are unresolved by modern simulations. At the massive end, the central problem is how to quench star formation to form the population of elliptical galaxies found in the local Universe and the ‘red sequence’ galaxies observed out to $z \geq 2$. The most massive ellipticals have high α/Fe abundance ratios implying very short formation times ($\Delta t \lesssim 1$ Gyr; Thomas et al. 2005, 2010).

The ejective feedback that is necessary to quench star formation quickly in simulations is predicted to be most effective in major mergers of massive gas-rich galaxies (e.g. Wuyts et al. 2010). Under the assumption that such mergers form dynamically hot spheroids and quench subsequent star formation (e.g. Springel, Di Matteo &

★E-mail: paul.sell@ttu.edu

Hernquist 2005), this merger-driven model has been proposed to be the dominant formation mechanism for red elliptical galaxies (Hopkins et al. 2008a). Feedback from an active galactic nucleus (AGN) is commonly invoked as the mechanism for heating up and driving out large fractions of cold gas, effectively quenching star formation (e.g. Granato et al. 2004; Hopkins et al. 2006; Menci et al. 2006; Booth & Schaye 2013). These models have been successful in reproducing a number of empirical trends, including the colour–magnitude relation and the correlation between SMBH mass and bulge stellar velocity dispersion. AGN feedback models accomplish this by assuming that ∼5 per cent of the radiated quasar luminosity can couple thermally and isotropically to the surrounding gas. However, linking galaxy-wide outflows to feedback processes (e.g. radiation pressure, jets) from an SMBH that originate on parsec scales remains a challenging problem because momentum coupling is not fully understood. Therefore, it is crucial to search for direct evidence of merger-induced quasar feedback. Unfortunately, even recent evidence for AGN feedback is still largely circumstantial (e.g. Cano-Díaz et al. 2012; Veilleux et al. 2013). Only in a limited number of cases, in very low redshift galaxies where powerful, kiloparsec-scale outflows can be resolved and examined in detail, can quasar feedback be most clearly traced back to the SMBH (e.g. Lipari et al. 2009; Greene et al. 2011; Rupke & Veilleux 2011; Greene, Zakamska & Smith 2012; Hainline et al. 2013).

Several observational studies have found that massive, quiescent galaxies at $z \sim 2$–3 are remarkably compact, with sizes a factor of 4–6 smaller than local galaxies (Trujillo et al. 2007; Zirm et al. 2007; Buitrago et al. 2008; van Dokkum et al. 2008). Highly dissipational mergers between gas-rich progenitors, which are more common at high redshift, have been invoked to explain these supercompact massive galaxies (Covington et al. 2011). It has been suggested that these massive galaxies evolve ‘inside out’ in order to arrive on the local size–mass relation (Hopkins et al. 2009b; Fan et al. 2013; van de Sande et al. 2013). There have been considerable recent efforts to identify the $z \sim 3$ star-forming progenitors of massive, compact, quiescent galaxies (Patel et al. 2012; Barro et al. 2013; Stefanon et al. 2013). Studying such faint systems in sufficient detail to gain insight into the physical mechanisms responsible for shutting down their star formation is very difficult at these redshifts. By identifying and studying lower redshift analogues, we may be able to more readily learn about higher redshift massive galaxy evolution.

With the preceding ideas in mind, we have been studying a sample of massive galaxies ($\log(M_*/\mathrm{M}_\odot) = 10.5$–11.5) at $z = 0.40$–0.75 selected to be in the midst of star formation quenching. They have very blue B- and A-star dominated stellar continua but relatively weak nebular emission lines (Hβ EW < 12 Å). Tremonti, Moustakas & Diamond-Stanic (2007) inferred that the star formation rate (SFR) in the last 10 Myr was significantly lower than it was in the past 100 Myr, and labelled them young post-starburst galaxies. Subsequent rest-frame mid-infrared (MIR) measurements revealed large luminosities, which might be explained if these galaxies are unusually compact young post-starbursts (Groves et al. 2008). However, modelling of the ultraviolet (UV) to near-IR (NIR) spectral energy distribution (SED) suggests a high level of heavily obscured star formation (Diamond-Stanic et al. 2012). In either case, the galaxies are very different from classic post-starburst galaxies (i.e. E+A or K+A galaxies; Dressler & Gunn 1983; Zabludoff et al. 1996; Poggianti et al. 1999), which do not exhibit such unusual properties and have been shown to have very little obscured star formation (Nielsen et al. 2012). Therefore, the galaxies in our sample are likely to be very close to their peak SFR, when quenching processes are expected to be the most active. Notably, two-thirds of the galaxies exhibit ≥1000 km s^{-1} outflows (Tremonti et al. 2007), the largest outflow velocities observed in star-forming galaxies at any redshift, suggesting that feedback may play a significant role in quenching.

We present detailed multiwavelength analysis of a small subsample of these galaxies. The 12 galaxies in this study are a subset of the 29 galaxies initially considered by Diamond-Stanic et al. (2012). They presented the basic result that many of these galaxies have compact morphologies (as small as $r_e \sim 100$ pc). The compact morphologies of these galaxies suggested that their high-velocity outflows could have been driven by extreme star formation feedback (Heckman et al. 2011).

Diamond-Stanic et al. (2012) highlighted the UV through infrared (IR) SEDs, *Hubble Space Telescope* (*HST*) images, and optical spectra for three galaxies with extraordinarily high SFR surface densities (up to $\Sigma_{\rm SFR} \approx 3000$ M$_\odot$ yr^{-1} kpc^{-2}) that approach the theoretical Eddington limit (Lehnert & Heckman 1996; Meurer et al. 1997; Murray, Quataert & Thompson 2005; Thompson, Quataert & Murray 2005). One of these galaxies, J1506+54, which is one of the 12 galaxies in our subsample, has also been investigated by Geach et al. (2013). Their recent CO observations of this galaxy indicate that it contains ∼10^{10}M$_\odot$ of cold gas. However, the very high $L_{\rm IR}/L_{\rm CO}$ ratio implies that it is being consumed with near 100 per cent efficiency, and will be exhausted in a few tens of Myr. Thus, we surmise that our galaxies are in the midst of starburst quenching.

An important issue is whether feedback from an AGN contributes to these outflows and whether the presence of an AGN could have affected the size measurements from *HST*. We consider whether the galaxies' recent activity is related to a merger, and we examine whether there is any evidence that the black hole (BH) plays a role in driving the fast outflows we observe and in quenching the starburst. For our investigation, we use multiwavelength diagnostics to build a comprehensive view of these galaxies. We combine targeted MMT UV–optical spectroscopy, *Chandra* X-ray observations, *HST* optical imaging, Jansky Very Large Array (JVLA) radio observations, and *Spitzer Space Telescope* (Werner et al. 2004) NIR imaging with survey imaging from the *Galaxy Evolution Explorer* (*GALEX*; Martin et al. 2005), Sloan Digital Sky Survey (SDSS; York et al. 2000), and *Wide-field Infrared Survey Explorer* (*WISE*; Wright et al. 2010).

This paper is organized as follows. Our sample selection is discussed in Section 2; data reduction and basic analysis of our multiwavelength observations is presented in Section 3 and in the appendix. Readers wishing to go straight to the results are encouraged to begin reading from Section 4, which provides a summary of the preceding analysis. In this section, we estimate the accretion rate of the three broad-line AGN and consider the available evidence for AGN activity in the other nine galaxies. We also include a case study of a galaxy in our sample with one of most extreme starbursts currently known (Section 4.2.2). In Section 5, we summarize the *HST* morphological analysis and highlight the very high star formation surface densities implied by the compact sizes of the galaxies. We assess whether AGN feedback is responsible for starburst quenching and the ultrafast outflows in our sample. Finally, we summarize this work and state our most important conclusions in Section 6.

Throughout this paper, we adopt the AB magnitude system, unless otherwise noted, and standard cosmological parameters: $H_0 = 70$ km s^{-1} Mpc^{-1}, $\Omega_{\rm M} = 0.3$, and $\Omega_\Lambda = 0.7$.

2 SAMPLE SELECTION

The parent sample from which our targets are drawn was selected from the SDSS Data Release 4 (Adelman-McCarthy et al. 2006).

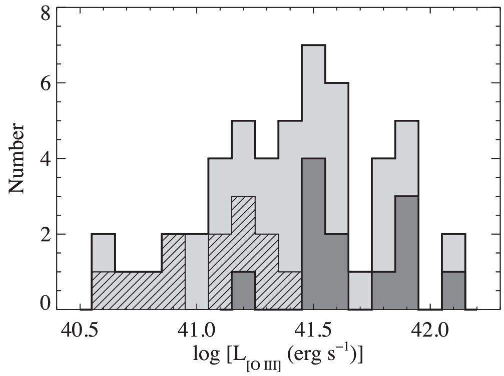

Figure 1. [O III] λ5007 luminosities of the 51 galaxies with spectroscopic follow-up (light grey). Data that are upper limits are shown with hatched lines overlaid. The subsample of 12 galaxies studied here is shown in dark grey. These galaxies sample the upper half of the [O III] luminosity distribution.

It is composed of $i < 20.5$ mag objects that were targeted for SDSS spectroscopy as low-redshift quasar candidates but were subsequently classified as galaxies at $z = 0.4$–1 by the SDSS spectroscopic pipeline. We used the low signal-to-noise ratio (S/N ∼ 2–4 per pixel) SDSS spectra to select 159 galaxies with post-starburst characteristics – strong stellar Balmer absorption and weak nebular emission. Fits to the rest-frame UV through NIR SEDs imply that the galaxies are massive ($M_* = 10^{10.5}$–$10^{11.5}$ M$_\odot$; see Section 3.6); thus, they are likely to host SMBHs.

We obtained higher S/N optical spectra of 51 of the galaxies with the MMT Blue Channel spectrograph and other facilities (see Tremonti et al. 2007, and Section 3.1 for details.). The spectra are dominated by the light of the host galaxy, but in some cases there is evidence suggestive of AGN activity. Some galaxies have [O III] λ5007/Hβ emission-line ratios that are higher than expected in massive galaxies that are purely star forming (see Section 4.2), and three of the galaxies show broad Mg II λλ2796, 2804 emission lines. To explore the possible SMBH activity in these sources, we selected the 12 galaxies with the strongest AGN signatures for follow-up with *HST* and *Chandra*. We included all three of the galaxies displaying broad Mg II emission (expected to be type I AGN) and nine additional galaxies with strong [O III] emission, which could be indicative of an obscured (type II) AGN. At the time of our *Chandra proposal*, these galaxies represented the most [O III]-luminous galaxies in our sample with spectroscopic follow-up. At present, the *Chandra* sample represents roughly half of the galaxies with $L_{[O\,III]} > 10^{41.5}$ erg s^{-1} (Fig. 1).

The galaxy coordinates, redshifts, and identification numbers that we use in the text and figures are provided in Table 1. This table also includes stellar mass estimates for the sample based on fitting the broad-band UV, optical, and NIR photometry using the Bayesian SED modelling code ISEDFIT (Moustakas et al. 2013), as described in Diamond-Stanic et al. (2012).

3 DATA REDUCTION AND ANALYSIS

3.1 MMT optical spectra

We obtained high S/N optical spectra of our galaxies with the Blue Channel spectrograph on the 6.5 m MMT between 2004 December and 2007 July. We used the 500-line mm grating blazed at 5600, which provided spectral coverage from approximately 4050–7200 Å with a dispersion of 1.19 Å pixel^{-1}. For our $z \sim 0.5$ galaxies, this yielded rest-frame coverage of 2700–4800 Å. We observed the galaxies using a 1 arcsec long slit, which yielded a full width at half-maximum (FWHM) resolution of 3.6 Å. Typical exposure times were 45–90 min. The resulting spectra have an S/N of 15–30 per pixel. The spectra were reduced, extracted, and spectrophotometrically calibrated using the ISPEC2D data reduction package (Moustakas & Kennicutt 2006).

The main motivation for the MMT spectra was to obtain higher S/N measurements of the Mg II λλ2796, 2804 interstellar medium (ISM) lines to look for evidence of gas outflows. We detected interstellar Mg II absorption in 3/4 of the spectroscopic follow-up sample and determined that it is blueshifted with respect to the starlight indicating gas outflows. Tremonti et al. (2007) reported line centroid velocities ranging from −573 to −2022 km s^{-1} and highlighted the fact that these outflows are a factor of 2–5 times faster than the outflow velocities of typical IR-luminous starburst galaxies (LIRGs and ULIRGs; e.g. Martin 2005; Rupke, Veilleux & Sanders 2005).

The spectra and the continuum-normalized Mg II lines are shown in Fig. 2. In the 9/12 cases, where Mg II absorption is observed, the doublet shows complex velocity structure and evidence of multiple line components. In this work, we characterize the outflow velocities in a slightly different manner than in Tremonti et al. (2007) to avoid the uncertainties inherent in fitting blended line components. To compute the average velocity of all line components, we measure the cumulative equivalent width (EW) distribution as a function of velocity. The velocity is defined relative to the average wavelength of the doublet ($\lambda_{avg} = 2799.12$) on the assumption that Mg II is saturated and thus the 2796 and 2804 lines contribute roughly equally to the absorption. The velocity at which the cumulative EW reaches 50 per cent is reported as v_{avg} in Table 1. We define the maximum velocity, v_{max}, as the velocity of the λ2796 line, at the point where the EW distribution reaches 98 per cent of the total. The value of v_{max} is reported in Table 1, and indicated by a vertical blue line in Fig. 2. In general, v_{avg} and v_{max} are highly correlated (Pearson $r = 0.87$) with v_{max} being larger by a factor of ∼1.4. The median values for the sample are $v_{avg} = -1040$ km s^{-1} and $v_{max} = -1490$ km s^{-1}. Determining whether these fast outflows are driven by starbursts or AGN is the main motivation for this work.

The MMT spectra agree extremely well with the SDSS spectra where there is overlap. We therefore join the MMT and SDSS spectra in order to extend our spectral coverage redwards to include the Hβ and [O III] λ5007 nebular emission lines. The combined spectra are shown in Fig. 2.

To measure the nebular emission lines, we first model and subtract the stellar continuum following Tremonti et al. (2004). This is particularly important for the Hβ line because of the strong underlying stellar Balmer absorption in our galaxies. We model the continuum using a linear combination of 10 single-age stellar population models. At optical wavelengths, we use the Charlot & Bruzual (2007) models (Bruzual 2007) which are an updated version of the models presented in Bruzual & Charlot (2003). At wavelengths less than 3600 Å, we use a custom grid of simple stellar population models built using the UVBLUE theoretical stellar library (Rodríguez-Merino et al. 2005). We adopt the Charlot & Fall (2000) dust attenuation curve and treat dust attenuation as an additional free parameter.

In the three cases where broad Mg II emission from a type I AGN is evident, we include an additional quasar template in our fitting. One well-known issue with the SDSS quasar composite spectrum (Vanden Berk et al. 2001) is that the optical portion of the spectrum was built from low-luminosity quasars and therefore it has some host galaxy contamination. To avoid this problem, we built

Table 1. General sample information.

ID	Galaxy	RA	Dec.	z	$\log(M_*)$	v_{avg}	v_{max}
		(J2000)			($M_\odot$)	(km s^{-1})	
(1)	(2)	(3)	(4)	(5)	(6)	(7)	(8)
1	J0826+43	126.660 04	43.091 51	0.604	10.8	−1230	−1500
2	J0944+09	146.074 38	9.5053 8	0.514	10.5	−1330	−1860
3	J1104+59	166.156 08	59.777 67	0.573	10.6	−1040	−1490
4	J1506+54	226.651 25	54.039 14	0.609	10.7	−1480	−2200
5	J1506+61	226.515 33	61.530 03	0.437	10.2	−1000[a]	−800
6	J1558+39	239.546 83	39.955 79	0.403	10.6	−1000	−1220
7	J1613+28	243.385 54	28.570 77	0.450	11.2	−1520	−2440
8	J1713+28	258.251 63	28.285 62	0.577	10.8	−930	−1190
9	J2118+00	319.600 25	0.291 50	0.460	11.1	–	–
10	J1359+51	209.837 42	51.627 48	0.413	10.5	–	–
11	J1634+46	248.693 71	46.329 65	0.576	11.8	–	–
12	J2140+12	325.002 04	12.154 06	0.752	10.9	−490	−950

Note. Column 1: galaxy identification number used in some figures for brevity. Column 2: abbreviated IAU designation used throughout the text. Columns 3 and 4: RA and Dec. in decimal degrees. Column 5: redshift. Column 6: stellar mass (uncertainties are approximately a factor of 2). Column 6 is based on SED fits assuming a Chabrier (2003) IMF from 0.1 to 100 $M_\odot$. Columns 7 and 8: the average and maximum outflow velocities (see Section 3.1 for details). No Mg II λλ2796, 2804 outflows were detected in 3/12 of the galaxies in this sample. Galaxies are ordered by their short name except the three galaxies with broad Mg II λλ2796, 2804 emission lines. These are placed at the end of the list because they are analysed separately.

[a]In J1506+61, strong emission-line in-filling of the Mg II absorption line causes the average velocity to be biased to larger negative values; the maximum velocity is less affected.

our own quasar-composite spectrum using the SDSS Data Release 7 data (Abazajian et al. 2009) and the quasar catalogue of Shen et al. (2011). To best match our type I AGN, we selected non-broad absorption line quasars with Mg II FWHM = 35–85 Å. To insure minimal host contamination, we additionally required the quasars to be moderately luminous ($L_{3000} > 10^{45}$ erg s^{-1}). Our composite spectrum is nearly identical to the Vanden Berk composite bluewards of 4000 Å, but at redder wavelengths, it has a steeper (bluer) slope due to the reduced host galaxy contribution. We include our quasar composite spectrum as an additional continuum template. This enables us to decompose the quasar and starlight in the spectrum and to estimate the quasar's luminosity (Table 5).

Our model of the stellar continuum and quasi-stellar object (QSO) continuum, if present, is shown in red (blue) in Fig. 2. We consider the [O III] luminosity and [O III]/Hβ ratio along with other multi-wavelength diagnostics of AGN activity in Section 4.

3.2 *HST* optical observations

All 12 galaxies were observed with the Wide Field Camera 3 (WFC3; Kimble et al. 2008) Ultraviolet Imaging Spectrograph channel using the *F*814*W* filter (Lupie & Boucarut 2003) aboard *HST*. The observations were dithered in a two-step sequence 1.49 arcsec apart. We used the on-the-fly reprocessing (Swade, Hopkins & Swam 2001) for the basic reduction and calibrations, but we reprocessed the images with multidrizzle (Jedrzejewski et al. 2005) to resample the images to a smaller pixel size (0.02 arcsec pixel^{-1}) and drop size (0.8) so that they have an rms value in the centre of the weight image $\lesssim$20 per cent the median value, as recommended in the Multidrizzle handbook.[1]. We experimented with a grid of values of these two parameters and found that these provided the best sampling relative to the rms.

We present 30 kpc × 30 kpc cutouts of our reduced galaxy images in Fig. 3. (See the appendix for additional images.) All of the galaxies show a bright, compact central source and are surrounded by irregular diffuse emission. In several cases, the galaxies show clear tidal tails indicative of late-stage major or minor mergers.

In 5/12 galaxies, the dominant central source is so compact that the structure of the *HST* point spread function (PSF) is faintly visible, suggesting that the galaxies are nearly unresolved. This is remarkable considering that typical host galaxy half-light radii at $z \sim 0.5$ are 0.1–0.6 arcsec or ∼10–60 times the *HST* PSF FWHM (e.g. Cassata et al. 2011). To explore the compactness and the nature of the extended diffuse light further, we undertake quantitative image analysis.

3.2.1 *Quantitative image analysis with* GALFIT

To obtain quantitative morphological information about our galaxies, we employed GALFIT version 3 (Peng et al. 2002, 2010), a two-dimensional fitting algorithm. GALFIT optimizes the fit of various models to an image (e.g. Sérsic profile, exponential disc, Gaussian) after convolving each with a user-supplied PSF. Because the *HST* PSF is complex and temporally and spatially variable, care must be taken in constructing the PSF model when the sources of interest are near the resolution limit. The preferred method of generating a PSF is to observe a nearby bright star at the same position on the CCD as the science target immediately before or after the science exposure. Since we did not anticipate that our galaxies would be extraordinarily compact, we did not take separate PSF images concurrently with our data. However, after much experimentation, we arrived at a technique for generating an empirical PSF from moderately bright stars in our science images. Details are discussed in the appendix.

[1] http://stsdas.stsci.edu/multidrizzle/

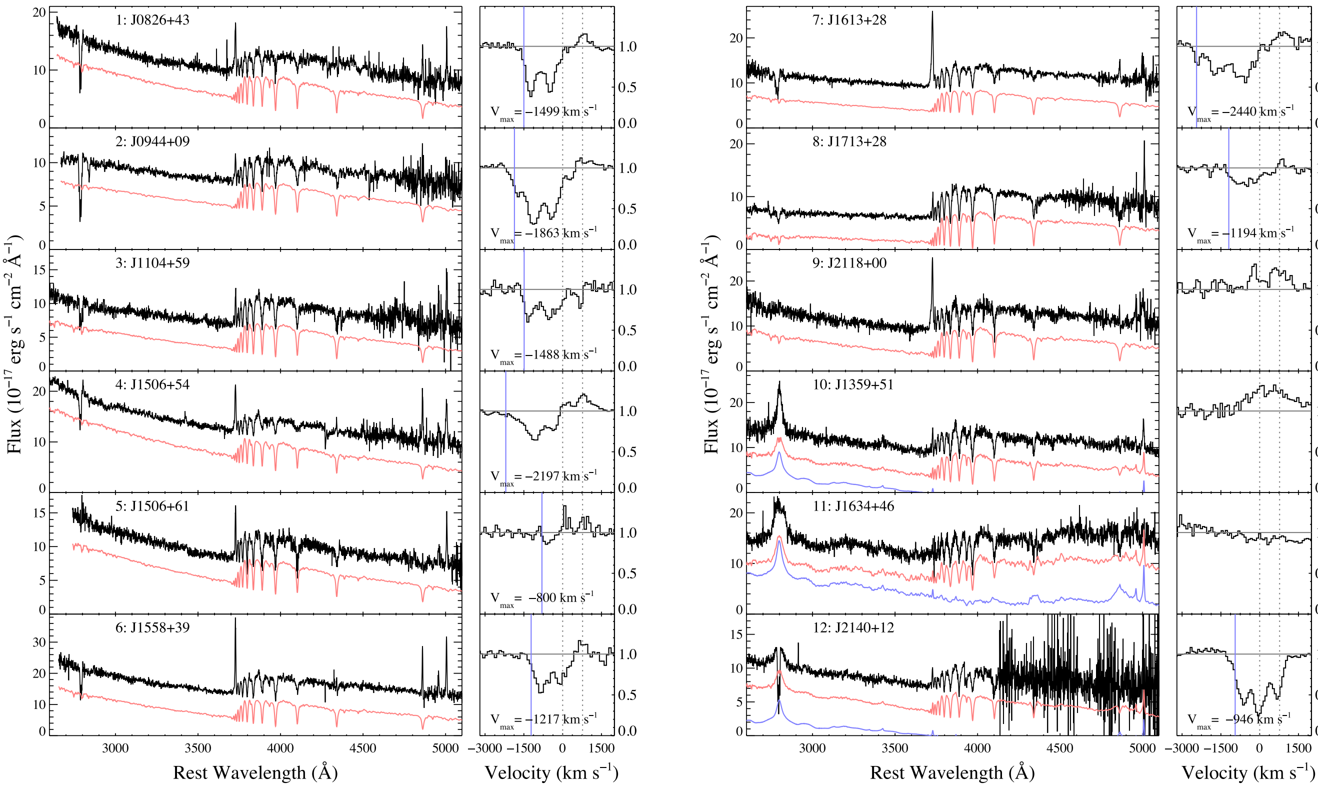

Figure 2. Rest-frame near-UV and optical spectra of the 12 galaxies. In the left-hand panel, the black line shows the combined MMT and SDSS spectrum (joined between 4100 and 5100 Å) and the red line shows the best-fitting model of the continuum, offset in the vertical direction for clarity. The continuum model is constructed from a custom grid of stellar population synthesis models (Section 3.1). Since J1359+51, J1634+46, J2140+12 show a broad Mg II emission line indicative of a type I (unobscured) AGN, an SDSS broad-line quasar composite spectrum was also included the fit (the blue spectra). The continuum model is subtracted from each spectrum before measuring the nebular emission lines of [O II] λ3727, Hβ, and [O III] λ5007. The region around the Mg II $\lambda\lambda$2796, 2804 lines is enlarged in the right-hand panel. In this panel, the continuum is normalized to unity and the x-axis indicates the velocity of the Mg II λ2796 line. The vertical dotted grey lines mark the rest-frame wavelength of the Mg II doublet and the blue line marks the maximum velocity (see Table 1 and Section 3.1). For 9/12 galaxies, strongly blueshifted interstellar Mg II is evident.

We fit each galaxy in a 1400 pixel × 1400 pixel cutout centred on the brightest core. This corresponds to 28 arcsec on a side or 151–206 kpc on a side for the range of redshifts in our sample. We measured radial profiles and visually inspected the images to verify that these boxes encompass all of the clearly associated diffuse merger emission (all radial profiles flatten out to the sky level). To mask the light from the background/foreground galaxies/stars, we used SExtractor (V2.8.6 Bertin & Arnouts 1996) to generate elliptical masks in the vicinity of our main target objects. After convolving the images with a Gaussian kernel with FWHM = 4 pixels, we detected objects using DETECT_THRESH between 1.5 and 3.0 and requiring DETECT_MINAREA=17 pixels. We were conservative in defining our object masks. We extended our masks out to five times the Kron radius measured by SExtractor in order to reach the background level. We inspected the ellipses within our cutouts, removing duplicate or spurious ones, increasing the ellipse sizes in a few extended haloes, and added polygons to encompass image artefacts. We then used the ellipses and polygons to create image masks for each of our galaxy cutouts. The images used in the fitting, radial profiles, and residual images are provided in the appendix in Fig. A3.

GALFIT provides the option of fitting the sky simultaneously with the galaxy model light profile. However, our galaxies contain diffuse tidal features that are not well modelled by the simple galaxy light profiles we assume, and these can skew the sky determination. Therefore, we opt to measure the sky independently and freeze it in our fits. We created radial profiles from our masked cutout images. Then, we determined by-eye where the radial profile became effectively flat and took this to be the sky region. Since careful inspection showed no evidence of sky gradients, we averaged all the unmasked pixels in this radial bin (over a million per galaxy) to determine the sky level.

We fit these galaxies with simple, physically motivated model combinations. We began by fitting each distinct, bright galaxy core with a Sérsic (Sérsic 1963) + sky model (where all sky model parameters were frozen). For the two galaxies with two distinct, clearly associated, bright cores, in the process of major or minor mergers, J1506+61 and J1713+28, we fit each core with a Sérsic profile. To accommodate the bright, compact cores of our galaxies, we also tried fitting each core with a Sérsic + PSF + sky model (again, all sky model parameters were frozen). In the case of the two galaxies with two distinct, clearly associated, bright cores, J1506+61 and J1713+28, we only added a PSF to the secondary core if there is a noticeable improvement to the fit (relatively large change in χ^2/ν) and if the best-fitting PSF magnitude was non-negligible (the PSF magnitude had to be $\gtrsim$1 per cent of the Sérsic magnitude). This requirement was only satisfied for J1713+28.

For the galaxies with visible broad-line regions (BLRs; J1359+51, J1634+46, and J2140+12), the PSF component can be used to model unresolved light from the AGN accretion disc.

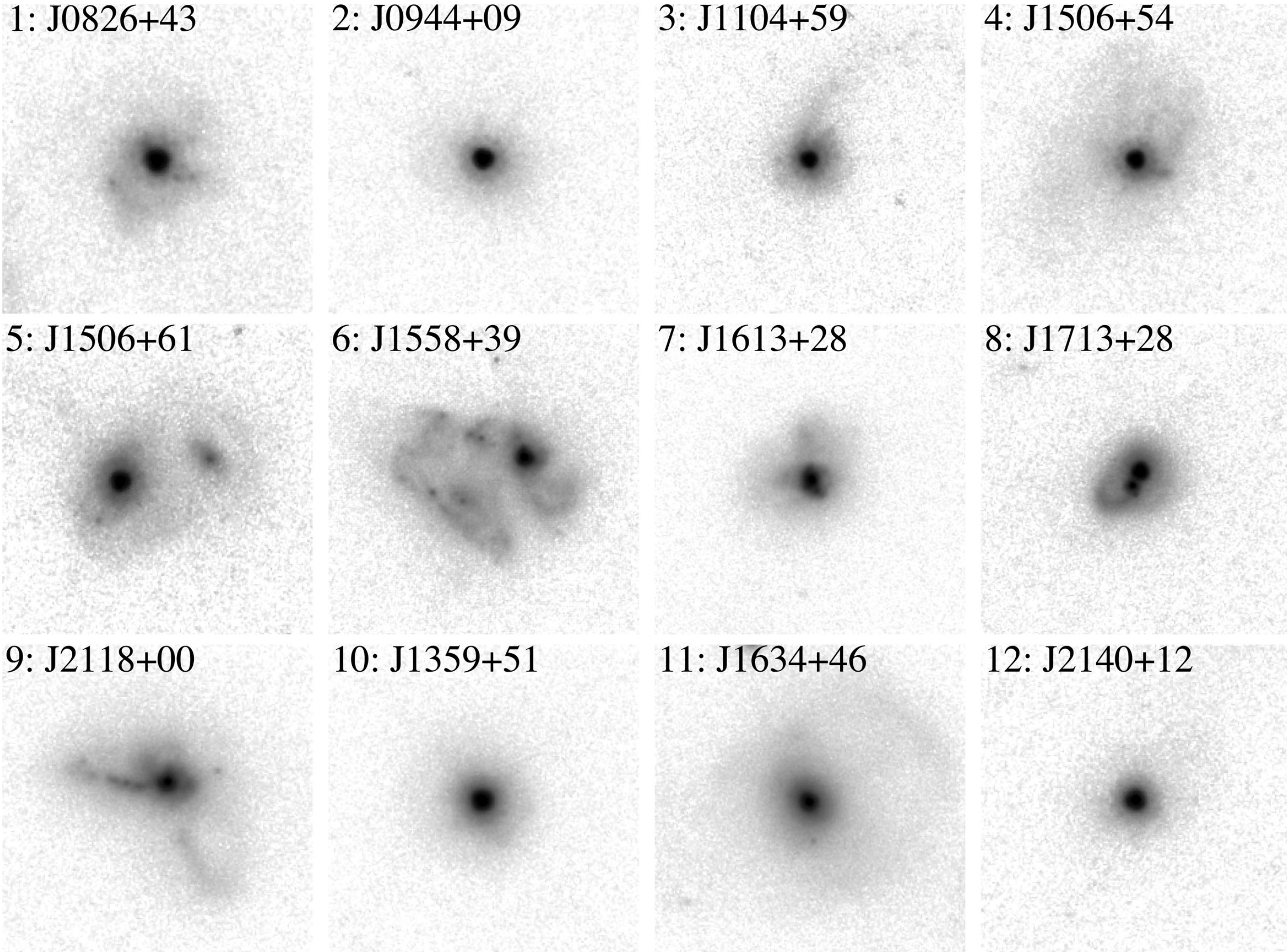

Figure 3. 30 kpc × 30 kpc cutouts from the *HST*/WFC3 *F*814*W* (rest-frame *V* band at these redshifts) observations of our 12 galaxies. The images are logarithmically scaled using the best-fitting sky level and Sérsic magnitudes to define the lower and upper scaling limits, respectively. North is up and east is left.

Our spectroscopic analysis suggests that the AGN should account for not more than 30–35 per cent of the continuum in the *HST* image. For the remainder of the galaxies, the PSF component could be used to model extremely compact star-forming regions (see Section 5.2 for further discussion.) We found that considering any more components beyond a Sérsic + PSF model per core was not physically justifiable and was technically intractable: considerable parameter degeneracies were encountered, GALFIT became more easily stuck in local minima, and the fits became very sensitive to the starting parameters.

To quantitatively assess whether a merger is major or minor, we use the integrated light ratios from the GALFIT results (the total integrated magnitudes in Table 2). First, J1713+28 appears to be a near-equal-mass major merger with two distinct nuclei with an integrated light ratio of 1.2. However, the light ratio is skewed by the way GALFIT defines the two cores (the first is very compact, while the second is much more extended and includes some of the tidal debris; see Table 2). These nuclei are linked by a small-scale tidal tail and appear to be separated less than a few kpc. Secondly, J1506+61 appears to be an ongoing merger with a much fainter companion core ∼10 kpc away and clearly associated tidal debris ∼70 kpc away on the opposite side of the galaxy from the companion. The integrated light ratio of 1.05 is also biased similarly to J1713+28 without including a PSF model. However, when a PSF is included for the primary core, the bias apparently disappears and we find an integrated light ratio of 4.9. Therefore, this galaxy appears to be a minor merger.

We explored fitting one more galaxy in the sample with a second Sérsic. J1634+46 has a second bright core ∼20 kpc away. If this core is associated with tidal debris near the primary core, it would clearly be a minor merger with an integrated light ratio of 37. While this core is projected within the very faint diffuse emission surrounding the primary core (see Fig. 4), there is no other clear morphological link between it and the merger remnant, suggesting that it could be a chance projection of a faint background galaxy. Therefore, we have chosen not to fit this core with a second Sérsic model. Not fitting this core does not affect our GALFIT results for the primary core.

For these two models, we experimented with either floating or fixing various model parameters. In particular, we experimented with allowing the Sérsic index, n, to float versus being frozen at common values of $n = 1$ (exponential) or 4 (de Vaucouleurs). However, the profiles were so peaked with relatively extended wings that the best-fitting Sérsic index always floated well beyond $n = 4$ up to the parameter space maximum allowed by GALFIT of $n = 20$. In addition, when the Sérsic index floated, the estimate of the effective

Table 2. Quantitative morphological fitting results.

ID	Galaxy	Sérsic only				Sérsic + PSF					
		Sérsic mag	R_e (pix)	R_e (pc)	Per cent resid	Sérsic mag	PSF mag	PSF frac	R_e (pix)	R_e (pc)	Per cent resid
(1)	(2)	(3)	(4)	(5)	(6)	(7)	(8)	(9)	(0)	(11)	(12)
1	J0826+43	19.23	1.60	214	38	19.50	19.64	0.47	39	5200	10
2	J0944+09	19.28	1.08	133	31	19.95	19.65	0.57	23	2800	14
3	J1104+59	19.25	1.68	219	20	19.80	19.79	0.50	15	2000	5
4	J1506+54	19.06	1.08	165	35	19.25	19.38	0.47	54	7300	3
5	J1506+61	19.45	1.92	217	4	19.69	19.99	0.43	28	3200	5
		19.50	165[a]	18 700		20.80			48	5400	
6	J1558+39	19.05	7.74	827	48	18.6	20.1	0.20	71	7600	7
7	J1613+28	18.69	8.55	980	17	18.72	22.27	0.04	9.6	1100	16
8	J1713+28	19.69	1.32	173	8	19.9	21.2	0.23	2.6	340	1
		19.46	28.6[a]	3760		19.5	22.2	0.08	47[a]	6200	
9	J2118+00	18.73	19.3[b]	2240	19	18.71	21.25	0.09	31	3600	10
10	J1359+51	18.87	3.24	352	17	19.19	20.00	0.32	9.3	1000	9
11	J1634+46	18.47	12.4	1630	37	18.40	20.09	0.17	37	4900	19
12	J2140+12	19.48	1.71	251	15	20.13	20.12	0.50	8.9	1300	8

Note. Column 1: galaxy identification number used in some figures for brevity. Column 2: SDSS short name. Columns 3 and 7: best-fitting Sérsic magnitude for each model. Columns 4, 5, 10, and 11: best-fitting Sérsic effective radius in *HST* pixels (0.02 arcsec pixel^{-1}) and parsec. Columns 6 and 12: per cent of light in the residual image. Column 8: best-fitting PSF magnitude. Column 9: the fraction of light in the PSF, $\mathrm{psf_{frac}}$ is defined as $\mathrm{psf_{flux}}/(\mathrm{Sérsic_{flux}} + \mathrm{psf_{flux}})$, which is a proxy for how PSF dominated or how well the galaxy is resolved. We freeze the Sérsic index, *n*, to 4 in all fits. We discuss why we choose not to provide parameter uncertainties in the appendix.

[a]These values of the effective radius for the second core are unusually large because the best-fitting r_e to the primary core is very small, requiring the second Sérsic to fit to the larger scale galactic emission. In particular, for J1506+61, once a PSF is added to the primary core, the Sérsic fit to that same core then fits most of the larger scale galactic emission. The fit is clearly much better when a PSF is added to the primary core for this galaxy.

[b]J2118+00 has the largest single Sérsic effective radius in the sample because bright tidal arms are superimposed on the core.

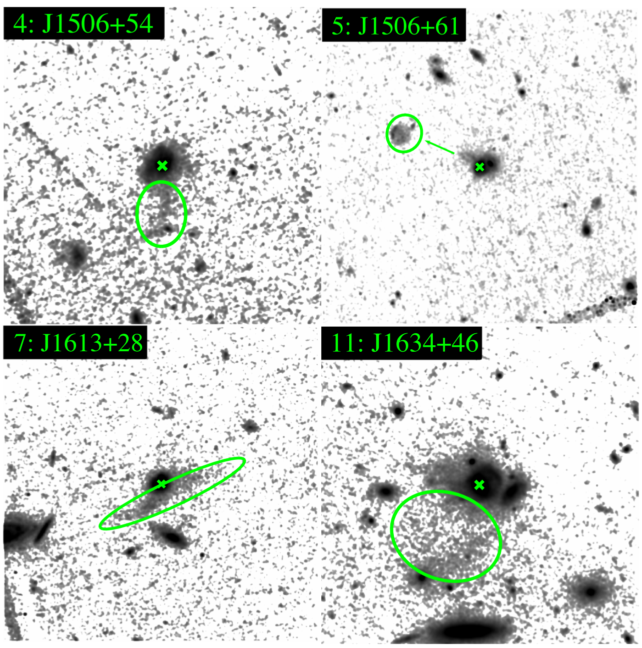

Figure 4. Additional very faint diffuse emission that appears to be associated with a few galaxies, which is not shown in cutouts elsewhere. The images have been binned 2 × 2, smoothed and filtered with IDL's LEEFILT, then smoothed again with a 5-pixel wide Gaussian kernel. The very straight lines in the corners of the images are artefacts. The centre of each galaxy has been marked with an 'X' and the extended diffuse emission has been encircled with an ellipse. Each stamp is 230 kpc × 230 kpc. North is up and east is left.

radius of the galaxy became much less constrained, as expected. The combination of a compact central source and extended irregular diffuse structure is inherently difficult to model. The inner part of the Sérsic profile is unresolved, while the faint outer wings, which could in principle help constrain *n*, are contaminated by the diffuse tidal structures. We conclude that we cannot meaningfully measure both the effective radius and the Sérsic index simultaneously for any model combination. Therefore, we freeze the Sérsic index to 4 for all of our fits. Tests of measurements of effective radii at various Sérsic radii ($n \sim$1–5) indicate that freezing the Sérsic index to such values does not strongly bias the effective radius.

We still found that these simplifications were not enough to prevent GALFIT from sometimes running into unphysical or unusual regions of parameter space. Therefore, we made one more model simplification to reduce the number of free parameters, which we found did help GALFIT find reasonable minima. If we fitted a Sérsic and a PSF to a single core, we tied the centroids of the models together to reduce the number of free parameters. This was consistent with by-eye inspection of the images that the PSF seems to be centred very close to the same position as the resolved emission.

One additional issue with GALFIT is that the results can be sensitive to the choice of starting parameters, suggesting that GALFIT is finding a local rather than a global minimum. In order to explore this issue, we ran GALFIT using a large grid of possible starting parameters. We found that our Sérsic + sky fits were very robust, returning near identical values of the effective radius and total magnitude for most values of the starting parameters. The Sérsic + PSF + sky fits were considerably less robust, as the range of best-fitting model parameters had large dispersions. The best fit beginning from a single set of starting parameters was sometimes not the same as or even close to the globally minimized χ^2, indicating that GALFIT stopped at a local minimum. Further details may be found in the appendix.

The results of our GALFIT modelling are listed in Table 2. The values reported are for the model with the minimum χ^2 drawn from our large grid of models with different starting parameters. In this table, we provide the Sérsic and PSF magnitudes, effective radii, the percentage of light in the residual image, and the fraction of light that GALFIT finds for the PSF: $\mathrm{psf_{frac}} = \mathrm{psf_{flux}}/(\mathrm{Sérsic_{flux}} + \mathrm{psf_{flux}})$. These latter two quantities are useful because they highlight for each galaxy how much of the light can be fitted in the simple models (relatively how disturbed they are), how much of an improvement adding the PSF makes, and a quantitative measure for how compact, unresolved, or PSF-like the galaxies are to one another. We found that when the PSF flux is approximately greater than or equal to the Sérsic flux, the airy ring and diffraction spikes of the PSF become apparent.

The per cent residuals provided in Table 2 indicate the fraction of galaxy light that is not well fitted by our simple GALFIT models. The per cent residuals are calculated by summing the pixels in the residual and original sky-subtracted images and then taking the ratio. Only pixels that are unmasked and inside of the sky annulus are included in the sum. We caution that this method of characterizing the residuals can sometimes be misleading because negative and positive deviations in the residual image can cancel out. In all cases except one, the per cent residuals are smaller when including a PSF model, as expected, because the additional model provides more freedom for the fit and better matches what is frequently a large fraction of unresolved light. In J1506+61, the per cent residuals are smaller without the PSF because the Sérsic model oversubtracts the host galaxy and the negative residual cancels out some of the positive residuals from the tidal features. However, the radial profiles of this galaxy (see the appendix) clearly show that the model is better matched to the data when a PSF model is included.

3.2.2 *The search for very faint, diffuse, extended emission*

To explore the nature of the extended diffuse emission, we employed two different techniques. We utilized GALFIT to remove the smooth, high-surface-brightness features from the images, making the diffuse irregular emission more visible (see Fig. A3). Our second approach was to use an image-filtering technique called LEEFILT in IDL (Lee 1986) that helped considerably to smooth out image noise to bring out the faint, extended, diffuse emission. Examples of smoothed and filtered images are shown in Fig. 4. While the emission shown in this figure is as low as ∼10–50 per cent above the background, it is extended over hundreds of pixels, making it highly significant ($\gg 10\sigma$). The surface brightness of this emission (Fig. 4; $\mu \sim 25$ mag arcsec^{-2}) is approximately an order of magnitude fainter than the faint emission in the cutouts (Fig. 3). This appears to be the ‘fine structure’ and tidal debris from recent mergers discussed by Duc & Renaud (2013). Note that two images (J0826+43 and J2140+12) have very faint artefacts from internal camera reflections that we have masked in our analysis. Diffuse structure is evident in all the images with a wide range of morphologies (see also Fig. A3 in the appendix).

3.3 *Chandra* X-ray observations

The 12 targets in Table 1 were observed on the S3 chip of the Advanced CCD Imaging Spectrometer (Garmire et al. 2003) aboard the *Chandra X-ray Observatory* for a total of 95.78 ks, ∼5–13 ks each. Data were taken in timed exposure mode with the standard frame time at the default location on the S3 chip and telemetered to the ground in very faint mode. Data reduction and point source extractions were completed using CIAO version 4.2 (Fruscione et al. 2006) and ACIS EXTRACT version 2010-02-26[2] (AE; Broos et al. 2010), respectively.

To maximize our *Chandra* observing efficiency, exposure times were estimated from both the SMBH mass (using the stellar mass; to detect a source accreting at >1 per cent of Eddington) and L_{X} / $L_{[\mathrm{O\,III}]}$ scaling relations for type I AGN (Heckman et al. 2005) with an additional obscuring screen of 10^{22-23} cm^{-2}. The goal was to detect each source with ∼10–150 counts (0.5–8.0 keV). However, only two galaxies are clearly bright, type I AGN: J1359+51 and J1634+46, which are detected with 97 and 67 counts, respectively. The remaining 10 galaxies were either not detected or barely detected by *Chandra* (J2140+12 shows faint AGN broad-line Mg II emission, but is among those not detected by *Chandra*). 3 of these 10 galaxies had only four counts each (0.5–8.0 keV). Using these sources and the one-count sources (0.5–8.0 keV; J1506+54, J1506+61, J1558+39, J1613+28, J1713+28, J2118+00), we created a merged spectrum that we will use to ascertain the nature of the faint X-ray emission.

We use AE’s PROB_NO_SOURCE (section 5.10.3 of the AE user’s manual) to assess if these galaxies with four counts each are significant detections (the single count sources are consistent with the background). This statistic gives the probability that the observed counts in the source extraction region are background counts. Given the low background levels of the *Chandra* observations and, especially that we know the location of the source a priori, the probabilities of $\lesssim 10^{-6}$ are highly significant. Furthermore, the merged data support this conclusion. PROB_NO_SOURCE is extremely small and a Kolmogorov–Smirnov test (Kolmogorov 1941) between the merged source and background spectra ($p = 3.5 \times 10^{-7}$ for 0.3–9.886 keV) strongly suggests that the merged spectrum is different from the background.

For the two brightest sources, the source position was adjusted based on the mean position of the extracted counts to more accurately calculate the point source photometry. For the remaining sources where possible, we aligned our exposures using other sources within a few arcminutes of our target that are detected in both the *HST* and *Chandra* images. This adjustment for the faint or undetected sources resulted in a shift in the coordinates of the extraction region $\lesssim$1 arcsec, which is consistent with the combined expected astrometric accuracy of *Chandra* ($\lesssim$0.8 arcsec)[3] and *HST* (∼0.4–0.8 arcsec; Morrison et al. 2001).

We used SHERPA version 4.5 (Freeman, Doe & Siemiginowska 2001) to jointly fit the unbinned source and background spectra at 0.5–8.0 keV of each source and of our merged source and background spectra. We used the *C*-statistic for the fitting, which is similar to the Cash (1979) statistic but with an approximate goodness-of-fit measure. We used this statistical method for the fitting to avoid losing the little spectral information that we have for most of our spectra (e.g. Nousek & Shue 1989). Since degeneracies in the fit parameters will frequently arise for low-count sources, we implemented a simple fitting scheme. We fit each source spectrum with an absorbed power-law model (XSPHABS × XSPOWERLAW). The column density, N_{H}, was fixed at the Galactic foreground value (Dickey & Lockman 1990) for each source and the photon index, Γ, was fixed at 1.7, consistent with typical values found for AGN (e.g. Page et al. 2005) and X-ray binaries (XRBs; e.g. Sell et al. 2011).

[2] http://www2.astro.psu.edu/xray/docs/TARA/ae_users_guide/ae_users_guide.html
[3] http://cxc.harvard.edu/cal/ASPECT/celmon/

Table 3. *Chandra* X-ray observation data.

ID (1)	Galaxy (2)	*Chandra* obsID (3)	Exposure time (s) (4)	Src cnts (5)	Bkg cnts (6)	PNS (7)	$\log(L_X)$ (erg s^{-1}) (8)
1	J0826+43	11698	9902	0	0.046	1.0	<42.9
2	J0944+09	11702	6398	0	0.029	1.0	<42.9
3	J1104+59	11696	8265	0	0.030	1.0	<42.9
4	J1506+54	11699	10780	4	0.086	2.4×10^{-6}	$41.9^{+1.0}_{-1.0}$
5	J1506+61	11705	13263	1	0.047	0.046	<42.6
6	J1558+39	11706	6139	1	0.022	0.022	<42.8
7	J1613+28	11700	4982	4	0.043	1.6×10^{-7}	$42.2^{+0.8}_{-0.6}$
8	J1713+28	11703	5832	1	0.024	0.023	<43.2
9	J2118+00	11707	5655	4	0.055	4.0×10^{-7}	$42.5^{+0.4}_{-0.6}$
10	J1359+51	11697	8215	97	0.082	0.0	$43.6^{+0.1}_{-0.3}$
11	J1634+46	11704	4982	67	0.045	0.0	$44.0^{+0.3}_{-0.1}$
12	J2140+12	11701	11365	0	0.051	1.0	<43.1
M	M	M	46653	15	0.277	3.1×10^{-21}	$42.2^{+0.3}_{-0.4}$

Note. Column 1: galaxy identification number used in some figures for brevity. 'M' is the merged X-ray spectrum of all sources with 1–4 counts. Column 2: SDSS short name. Column 3: *Chandra* observation identification number. Column 4: exposure time of each *Chandra* observation. Column 5: counts in *Chandra* source extraction region enclosing 95 per cent of the PSF in the range 0.5–8.0 keV. Column 6: expected background counts in the source region from a nearby annular extraction. Column 7: PROB_NO_SOURCE: AE's probability that there is no source in the range 0.5–8.0 keV as defined in section 5.10.3 of the AE user's manual. Column 8: 2.0–10.0 keV *K*-corrected X-ray luminosity.

Each background spectrum was simultaneously fitted with a power law with $\Gamma = 1.4$, consistent with the hard-X-ray background (e.g. Tozzi et al. 2006). Note, however, that, because the background is very low, approximately half of the flux in the background region is instrumental.[4]

If we allow Γ to float for the two type I AGN and the merged source spectra, the best-fitting value is consistent with $\Gamma = 1.7$ within the uncertainties calculated by SHERPA's conf.[5] We also consider possible attenuation in these sources. Including intrinsic, redshifted absorption for these three sources does not change the luminosity more than 10 per cent as such a model strongly prefers low intrinsic $N_{\rm H}$; we find 3σ upper limits on the intrinsic $N_{\rm H}$ for J1359+51, J1634+46, and the merged spectrum, respectively (in units of 10^{21} cm^{-2}): 1.6, 5.6, and 4.9. For these three sources, $N_{\rm H}$ is 2–3 orders of magnitude smaller than expected for a highly obscured or Compton-thick AGN (e.g. Vignali et al. 2010). This is also supported by hardness ratio analysis of the merged spectrum. Using the BEHR code (Park et al. 2006), we calculate a hardness ratio, $(H-S)/(H+S)$, of $-0.58^{+0.30}_{-0.13}$ ($H = 2.0$–8.0 keV, $S =$0.5–2.0 keV). However, this value is not unexpected for XRBs, which can be a wide range of X-ray colours (e.g. Trouille et al. 2008, we return to this in Section 4.2.3). These results are consistent with the finding that these are relatively soft sources exhibiting very little intrinsic absorption.

For comparison to other studies, the 2.0–10.0 keV X-ray luminosities listed in Table 3 were calculated from each of the model fits and the uncertainties were calculated as follows. The luminosity is evaluated at each point in a 2D grid 200 points on a side, each dimension corresponding to the power-law photon index and power-law normalization. The absorption was frozen at the galactic foreground value and not allowed to vary since we can only constrain $N_{\rm H}$ in the type I AGN and merged sources; the type I AGN and merged source uncertainties were calculated in the same way for consistency. The photon index was allowed to vary 1.7 ± 0.4 to encompass the typical observed photon indices for AGN (e.g. Xue et al. 2011). Then the minimum and maximum luminosity was selected within the confidence interval for the appropriate change in statistic value (e.g. Avni 1976).

[4] http://cxc.harvard.edu/proposer/POG/html/chap6.html#tth_fIg6.21

[5] http://cxc.harvard.edu/sherpa/ahelp/conf.html

3.4 JVLA radio observations

Radio observations were obtained for 10 of the 12 galaxies with the JVLA in *C*-configuration during fall 2010. Observations were made using the *L*-band continuum mode with a spectral range of 1536–1664 MHz made up of 256 channels. We began each set of observations by looking at a bright flux calibrator followed by a phase calibrator. We then spent 80–90 min of total integration time on each target galaxy, alternating between the target and the phase calibrator every 20 min.

The observations were reduced using standard calibration techniques in CASA (Petry & CASA Development Team 2012).[6] Unfortunately, the radio frequency interference in our chosen wavelength regime required us to flag 60–80 per cent of the bandpass, which prevented us from achieving our target noise limit of 15 μJy beam^{-1}. Consequently, we achieved similar detection limits and uncertainties to the FIRST survey (Becker, White & Helfand 1995). We only detected one galaxy (J1634+46, one of the type I AGN) at the same flux level as FIRST. This galaxy is clearly a radio-loud AGN (see Table 4).

3.5 *WISE* IR observations

We derive the galaxies' rest-frame 12 μm luminosity from observed-frame 12 and 22 μm photometry from the *WISE* bands W3 and W4. We do not report results for J1104+59, which is contaminated by

[6] http://casa.nrao.edu/

Table 4. Supplemental multiwavength data

ID	Galaxy	$\log(L_{\rm R})$ (W Hz^{-1})	$L_{[\rm O\,III]}$ (10^{40} erg s^{-1})	$L_{[\rm Ne\,V]}$ (10^{40} erg s^{-1})	3.6–4.5 µm Colour	$L_{12\,\mu\rm m}$ (10^{44} erg s^{-1})	$\rm SFR_{IR}$ ($\rm M_{\odot}$ yr^{-1})
(1)	(2)	(3)	(4)	(5)	(6)	(7)	(8)
1	J0826+43	<23.39	72.9 ± 6.6	<6.6	0.18 ± 0.05	4.90 ± 0.49	380
2	J0944+09	<23.63	16.4 ± 3.3	<2.0	0.35 ± 0.05	3.81 ± 0.31	220
3	J1104+59	<23.73	73.3 ± 7.9	5.2 ± 1.2	–	–	70
4	J1506+54	<23.68	133.5 ± 6.0	16.3 ± 1.6	0.35 ± 0.05	11.77 ± 1.21	250
5	J1506+61	<23.41	32.2 ± 1.9	<2.1	0.28 ± 0.05	0.59 ± 0.05	210
6	J1558+39	<23.27	66.9 ± 2.2	<2.3	0.57 ± 0.05	2.69 ± 0.26	610
7	J1613+28	<23.40	31.8 ± 3.4	<2.8	0.61 ± 0.05	7.83 ± 0.98	230
8	J1713+28	<23.80	88.1 ± 5.7	4.2 ± 0.9	–	–	500
9	J2118+00	<23.39	43.4 ± 3.5	<5.2	0.57 ± 0.05	7.20 ± 0.76	130
10	J1359+51	<23.25	32.2 ± 2.1	6.5 ± 1.0	0.58 ± 0.05	0.71 ± 0.05	<350
11	J1634+46	25.14 ± 0.02	37.8 ± 8.3	13.1 ± 2.6	0.40 ± 0.05	1.42 ± 0.09	<400
12	J2140+12	<23.94	7.1 ± 15.2	<8.3	0.49 ± 0.05	7.63 ± 0.39	<500

Note. Column 1: galaxy identification number used in some figures for brevity. Column 2: SDSS short name. Column 3: *K*-corrected radio luminosity. Column 4: [O III] (λ5007) luminosity. Column 5: [Ne V] (λ3426) luminosity. Column 6: the IRAC 3.6−4.5 µm observed colour (Vega magnitudes). Column 7: *K*-corrected 12 µm luminosity. Column 8: IR-based SFR using the Kennicutt (1998) calibration converted to a Chabrier (2003) IMF. The uncertainties are approximately a factor of 2–3. The SFRs for the last three (broad-line AGN) are listed as upper limits because we have not accounted for an AGN contribution to the IR.

a nearby star, and J1713+28, which is not detected. The median S/N of the remaining sources is 7 and 3 for bands W3 and W4, respectively. We fit the data with a range of star-forming galaxy templates (for more details, see Diamond-Stanic et al. 2012). We consider templates from Chary & Elbaz (2001), Dale et al. (2005), and Rieke et al. (2009) and use the average of our results and the standard deviation of the three model values to estimate our errors. We also estimate the SFR from the IR using the Kennicutt (1998) calibration converted to a Chabrier (2003) initial mass function (IMF). Both the IR luminosities and SFRs are listed in Table 4.

3.6 Stellar masses

We derive stellar masses from the galaxies' 0.1–5 µm SEDs. We use far- and near-UV photometry from *GALEX* and *ugriz* optical photometry from the SDSS Data Release 8 (Aihara et al. 2011). We obtained 3.6 and 4.5 µm images with the Infrared Array Camera (IRAC; Fazio et al. 2004) as part of *Spitzer* GO programme 60145. We used the post-basic calibrated data to perform aperture photometry on all sources and point-source photometry on sources in crowded fields. The SED analysis is performed using ISEDFIT, a code which implements a simplified Bayesian framework to derive galaxy physical properties (Moustakas et al. 2013). A Chabrier (2003) IMF is assumed. Stellar masses are reported in Table 1. A more detailed description of the SED modelling of the broad-band spectra of these galaxies is beyond the scope of this paper and will be discussed in a future publication.

4 ASSESSMENT OF SMBH ACTIVITY

4.1 Broad-line AGN

The rest-frame optical spectrum of our targets is dominated by the light of the host galaxy (Fig. 2). However, 3 of the 12 galaxies (J1359+51, J1634+46, and J2140+12) display broad Mg II emission indicative of a type I AGN. For these sources, we obtain virial SMBH mass estimates from the Mg II linewidth and the AGN continuum luminosity at 3000 Å following Trakhtenbrot & Netzer (2012). We have been careful to decompose the continuum of the host galaxy and that of the AGN using stellar population synthesis modelling. Results are reported in Table 5.

The SMBH masses that we infer using the viral technique are large, $M_{\rm BH} = 10^{8-9}\,\rm M_{\odot}$. The masses are in reasonable agreement with the SMBH–stellar mass correlation (Marconi & Hunt 2003; McConnell & Ma 2013; Schramm & Silverman 2013). We detect J1359+51 and J1634+46 in X-rays, while J2140+12 is undetected (see Section 3.3 for details.)

We use the optical continuum light and X-rays separately to estimate the AGN bolometric luminosities. We use the luminosity-dependent bolometric corrections of Trakhtenbrot & Netzer (2012) for the optical and Brightman et al. (2013) for the X-rays. We calculate Eddington luminosities using $L_{\rm Edd} = (1.26 \times 10^{38})(M_{\rm BH}/\rm M_{\odot})$. We find ratios of ∼1–7 per cent of Eddington for these galaxies, which are typical for samples of broad-line AGN, but lower than typical SDSS quasars (Kelly et al. 2010; Steinhardt & Elvis 2010; Kelly & Shen 2013).

One surprising result is that J2140+12 is not X-ray detected, yielding a $L^{X}_{\rm bol}/L_{\rm Edd}$ 3σ upper limit for this broad-line AGN approximately two times lower than $L^{3000}_{\rm bol}/L_{\rm Edd}$. This could be explained by either variability between the time of the optical and X-ray observations, which is causally possible on these time-scales (e.g. Ulrich, Maraschi & Urry 1997; McHardy 2013), or by considerable differential attenuation by the large amounts of cold gas that could still be present shortly after a galaxy merger. There could be X-ray absorption from dust-free gas inside the dust sublimation radius (Maiolino & Risaliti 2007). In addition, since the X-rays are likely concentrated much more centrally than the Mg II λλ2796, 2804 broad-line emission and the UV continuum (e.g. in the case of a simple, disc blackbody model), a couple of high-density, au-scale gas clouds could more easily obscure the X-ray-emitting region as compared to the UV-emitting BLR. This could also explain the strong absorption dips seen in the broad Mg II line (see Fig. 2).

4.2 Narrow-line AGN or star-forming galaxies?

Nine of the 12 galaxies in the sample do not show evidence of broad Mg II or Hβ emission lines. Here, we use multiwavelength

Table 5. Properties of type I AGN.

ID	Galaxy	$f_{\mathrm{AGN,\,3000}}$	$f_{\mathrm{AGN},\,F814W}$	$\log L_{3000}$ (erg $\mathrm{s^{-1}}$)	Mg II FWHM (Å)	Mg II EW (Å)	$\log(M_{\mathrm{BH}}/\mathrm{M_{\odot}})$	$L_{\mathrm{bol}}^{3000}/L_{\mathrm{Edd}}$	$L_{\mathrm{bol}}^{\mathrm{X}}/L_{\mathrm{Edd}}$
(1)	(2)	(3)	(4)	(5)	(6)	(7)	(8)	(9)	(10)
10	J1359+51	0.62 ± 0.02	0.31 ± 0.05	44.16 ± 0.01	39.6 ± 1.0	$28.1^{+3.5}_{-2.9}$	8.10 ± 0.02	$0.068^{+0.068}_{-0.039}$	$0.042^{+0.041}_{-0.025}$
11	J1634+46	0.74 ± 0.09	0.30 ± 0.05	44.66 ± 0.05	82.2 ± 1.6	$43.0^{+4.7}_{-3.9}$	9.04 ± 0.04	$0.017^{+0.017}_{-0.010}$	$0.014^{+0.014}_{-0.009}$
12	J2140+12	0.58 ± 0.03	0.33 ± 0.05	44.64 ± 0.02	54.8 ± 0.7	$18.4^{+1.2}_{-1.1}$	8.65 ± 0.02	$0.037^{+0.037}_{-0.021}$	<0.018

Note. Column 1: galaxy identification number used in some figures for brevity. Column 2: SDSS short name. Column 3: fraction of the continuum light at 3000 Å contributed by the AGN. Column 4: fraction of the continuum light through the *F*814*W HST* filter contributed by the AGN. The values in columns 3 and 4 were estimated from the SED modelling. Column 5: AGN continuum luminosity at 3000 Å (λL_{λ}). Column 6: rest-frame FWHM of the broad Mg II line (fitted using a single Gaussian). Column 7: rest-frame EW of the broad Mg II line. Column 8: SMBH mass derived using equation 12 of Trakhtenbrot & Netzer (2012). Since the listed random error is much smaller than the approximate systematic error (0.32 dex; Trakhtenbrot & Netzer 2012), the systematic error is used to estimate the uncertainties in $L_{\mathrm{bol}}^{3000}/L_{\mathrm{Edd}}$ and $L_{\mathrm{bol}}^{\mathrm{X}}/L_{\mathrm{Edd}}$. This systematic error dominates the error budget in these two quantities. Column 9: ratio of the bolometric to Eddington luminosity. L_{bol}^{3000} is inferred from the optical continuum following Trakhtenbrot & Netzer (2012). Column 10: same as column 9 except that $L_{\mathrm{bol}}^{\mathrm{X}}$ is the bolometric luminosity estimated from L_{X} and L_{3000} using Brightman et al. (2013).

diagnostics to assess the relative contribution of star formation and obscured AGN activity to their bolometric luminosities.

4.2.1 *Optical narrow-line diagonsitcs*

The classic line ratio diagnostic diagram of [N II] (λ6584)/Hα versus [O III] (λ5007)/Hβ, commonly called the 'BPT' diagram, has been widely used as a diagnostic to separate star-forming galaxies and AGN (Baldwin et al. 1981; Veilleux & Osterbrock 1987) and various subclasses of AGN (Kewley et al. 2006). In Fig. 5(a), we show the BPT diagram for a sample of ~338 000 low-redshift galaxies drawn from the SDSS-I MAIN sample (Strauss et al. 2002). These galaxies have redshifts between $z = 0.02$ and 0.25 and stellar masses between $M_{*} = 10^{8.5}$and10^{12} $\mathrm{M_{\odot}}$. The solid line is the empirical dividing line proposed by Kauffmann et al. (2003) to separate pure star-forming galaxies from AGN. The dashed line is the theoretical maximum starburst limit proposed by Kewley et al. (2001). Galaxies falling between the solid and dashed lines are classified as 'composites' because most are believed to be ionized by a mixture of star formation and AGN activity. We do not have measurements of [N II] and Hα for our $z > 0.4$ galaxies. Their [O III]/Hβ fluxes are indicated at the right-hand edge of the BPT diagram by the galaxy ID number. $L_{[\mathrm{O\,III}]}$ is listed in Table 4.

For comparison with our $z \sim 0.6$ galaxies, we select a subsample of SDSS-I MAIN galaxies that are comparably massive ($M_{*} > 10^{10.5}$ $\mathrm{M_{\odot}}$) and blue ($(U - B)_0 < 0.5$). In Fig. 5, the 33 star-forming galaxies that meet this criterion are shown in green and the 14 composites and AGN are shown as magenta points. Note that such galaxies are very rare at low redshift, comprising only 0.01 per cent of the parent sample. (The photometry and spectroscopy of the comparison galaxies has been hand checked to remove contaminants due to photometry errors from bright stars, etc.) Several alternate diagnostic diagrams have been devised for use at $z > 0.4$, where [N II] and Hα have redshifted out of the observed-frame optical (Lamareille 2010; Juneau et al. 2011; Trouille, Barger & Tremonti 2011; Yan et al. 2011). We show three of these diagnostics in Figs 5(b)–(d). These pseudo-BPT diagrams typically have difficulty in identifying composite sources that contain both significant star formation and AGN activity. To illustrate this, we have overplotted the SDSS-I composites in grey-scale. All panels also include the mass- and colour-matched comparison sample (green and magenta points).

Fig. 5(b) shows the 'Blue' AGN diagnostic (Lamareille 2010), which substitutes [O II]/Hβ for [N II]/Hα. To mitigate extinction effects on the widely separated [O II] and Hβ lines, this diagram uses the ratio of line EWs rather than line fluxes (this assumes that the attenuation of the continuum and emission lines is the same). In Fig. 5(c), we show the mass-excitation (MeX) diagram of Juneau et al. (2011), which substitutes stellar mass for the [N II]/Hα ratio. In this diagram, composites dominate the wedge-shaped region between the star-forming galaxies and AGN. Fig. 5(d) shows the colour-excitation (CeX) diagram of Yan et al. (2011) which utilizes the rest-frame $U - B$ colour in AB magnitudes in place of [N II]/Hα. The region between the star-forming galaxies and AGN was identified by Juneau et al. (2011) as being dominated by composite galaxies.

Based on these diagrams together, we classify J1713+28 (ID 8) as the most-likely galaxy to host a type II AGN, followed by J1104+59 (ID 3). To place the most likely galaxy (J1713+28 or ID 8) in context, we estimate the bolometric Eddington fraction using the measured [O III] luminosity in Table 4. Unfortunately, our bolometric estimate will be very uncertain because we do not have enough information to correct [O III] for extinction and we do not know how much the [O III] emission from an AGN is contaminated by star formation. The bolometric correction for [O III] typically ranges from 600 (Heckman et al. 2004) to 3500 (Kauffmann & Heckman 2009), depending on the extinction correction. From these conversions, we estimate $L_{\mathrm{bol,[O\,III]}} \approx 0.5$–$3 \times 10^{45}$ erg $\mathrm{s^{-1}}$. Then, using the SMBH–bulge mass relation of McConnell & Ma (2013) to estimate the SMBH mass and hence L_{Edd}, we find a rough estimate for the bolometric Eddington fraction: $L_{\mathrm{bol}}/L_{\mathrm{Edd}} \approx 0.02$–0.13. This estimate is comparable to the bolometric Eddington fractions found for the type I AGN in our sample (~1–7 per cent; see Table 5) and to J1506+54 (ID 4; see Section 4.2.2). The remaining seven narrow-line galaxies, along with the mass and colour-matched, low-z comparison sample, are classified inconsistently or ambiguously by the Blue, MeX, and CeX diagrams. For the low-z comparison sample, the MeX diagram does the best job of reproducing the BPT classifications, but still classifies over half of the BPT star-forming galaxies as AGN or composites.

This analysis indicates that the pseudo-BPT diagrams (Figs 5b–d) may not be reliable for certain types of galaxies. Future NIR spectroscopy of the sample will enable us to measure their [N II]/Hα ratios so that we can place them on the BPT diagram. However, recent studies indicate even BPT classification must be treated with

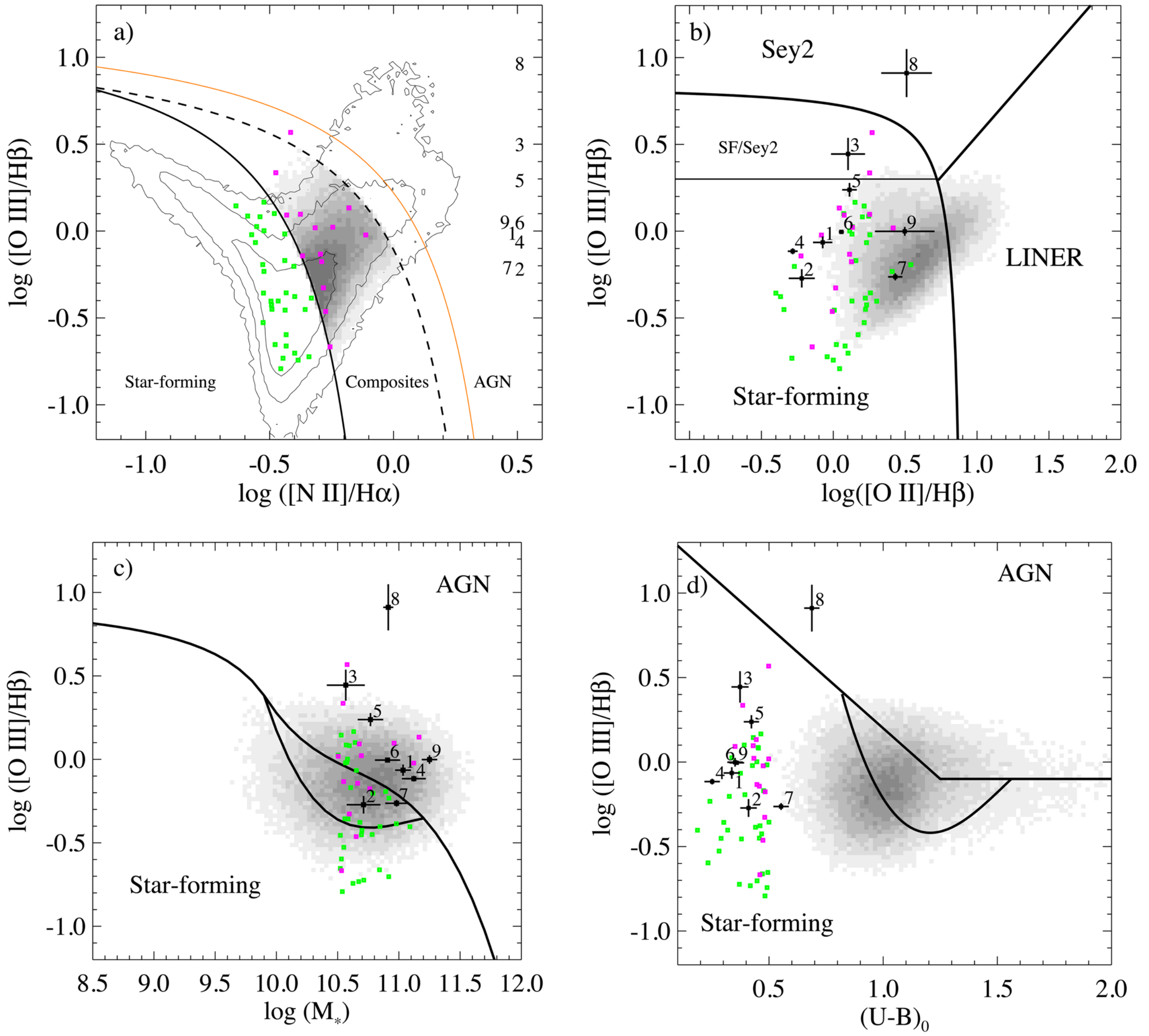

Figure 5. Diagnostic diagrams designed to separate star-forming galaxies, AGN (Seyfert 2s/LINERs), and composite systems. The nine galaxies with narrow emission lines are labelled with their galaxy ID number (Table 1). Panel (a) shows the BPT diagram (Baldwin, Phillips & Terlevich 1981) of ∼338 000 galaxies at $z = 0.02-0.25$ from the SDSS-I MAIN sample (contours). The black solid and dashed lines show the divisions between star-forming galaxies and AGN proposed by Kauffmann et al. (2003) and Kewley et al. (2001), respectively. The solid orange line shows the theoretical upper limit star-forming abundance sequence for $z = 3$ from Kewley et al. (2013b). Our $z > 0.4$ galaxies lack [N II]/Hα measurements; their [O III]/Hβ values are indicated at the right of the BPT diagram by their ID number. Panel (b) shows the 'Blue' diagnostic of Lamareille (2010); panel (c) the MeX of Juneau et al. (2011); and panel (d) the CeX of Yan et al. (2011). In all panels, BPT composites are shown in grey-scale. We highlight 47 SDSS-I MAIN galaxies that have masses and colours similar to our galaxies as green (BPT star forming) and magenta (BPT composite and AGN) points. J1713+28 (ID 8) is likely an AGN; the other eight galaxies are not consistently classified, nor are the galaxies in the comparison sample (green and magenta points). See Section 4.2.1 for details.

some caution. In fact, studies of rest-frame optical emission lines of star-forming galaxies at $z \sim 1$–2 (e.g. Shapley et al. 2005; Erb et al. 2006; Liu et al. 2008) have shown that high-z galaxies have elevated [O III]/Hβ ratios relative to local star-forming galaxies. The small fraction of local galaxies with similar line ratios tend to have larger electron densities, SFRs, and SFR surface densities (e.g. Kewley et al. 2001; Brinchmann, Pettini & Charlot 2008; Liu et al. 2008), which suggests that H II region physical conditions influence a galaxy's position on the BPT, sometimes leading to misclassification. This is particularly germane to our sample because we expect elevated electron densities and interstellar pressures in compact starbursts (Liu et al. 2008; Verdolini et al. 2013; Rich, Kewley & Dopita 2014).

A new set of theoretical models (Dopita et al. 2005, 2006b,a), which are compared to high-redshift samples, show how these types of galaxies move on the BPT diagram (Kewley et al. 2013a,b). Compact starburst galaxies at higher redshift, which have larger pressures and densities of ionizing photons, fall in the same position on the diagram as galaxies labelled as 'composites' at low redshift. In particular, some of the Groves et al. (2008) models predict log ([O III]/Hβ) ratios for some compact starbursts up to 0.9, statistically consistent with all of the [O III]/Hβ ratios in our sample.

Thus, it is not possible to draw firm conclusions at the present time about the nature of the excitation in any of the non-broad-line galaxies from these diagnostics.

4.2.2 SDSS J1506+54: a case study of a galaxy with [Ne V]

[Ne V] (λ3426) is typically an order of magnitude weaker than [O III] (Ferland & Osterbrock 1986), but it has a much higher ionization energy making it a valuable tracer of AGN activity (Schmidt et al. 1998).[7] Indeed, it is not too surprising that we strongly detect [Ne V] in the two X-ray-detected broad-line AGN (J1359+51 and J1634+46); the third broad-line AGN, J2140+12, may be strongly variable or likely suffers from considerable attenuation (see Section 4.1 and Table 4).

We detect [Ne V] in three of the nine narrow-line galaxies. The line is very strongly detected ($\sim 10\sigma$) in one of these galaxies (J1506+54) and is only weakly detected ($\lesssim 4\sigma$) in two other cases (J1104+59 and J1713+28). The significant detection of [Ne V] in the two latter galaxies is consistent with the finding in Section 4.2.1 that these galaxies are most likely to host obscured AGN activity. However, assessing the [Ne V] contribution in these latter two cases could be controversial and extremely challenging: (1) the significance and luminosity of the [Ne V] line is sensitive to the fit of the galaxy continuum model, which has an additional uncertainty not encapsulated above that is very difficult to quantify; (2) the measured strength of a line near the sensitivity limit can be overestimated (Rola & Pelat 1994); and (3) without an AGN, very young stellar populations containing Wolf–Rayet and other O stars (less than a few Myr) can produce some detectable [Ne V] because much higher fractions of high-energy photons are produced (Abel & Satyapal 2008). Given these challenges applied to our unusual galaxies, we only analyse the very strong detection of [Ne V] in J1506+54 in detail.

First, we consider the case where the narrow-line and X-ray emission is produced by an AGN. Gilli et al. (2010) suggest that the ratio of X-ray to [Ne V] luminosity is a good diagnostic of AGN nuclear obscuration. Following Gilli et al. (2010), we do not correct narrow-line emission for extinction. They found $L_X/L_{[\mathrm{Ne\,V}]} \sim 400$ for type I (unobscured) AGN and $L_X/L_{[\mathrm{Ne\,V}]} < 15$ for a Compton-thick AGN. We measure $L_X/L_{[\mathrm{Ne\,V}]} = 4.9$, which implies a Compton-thick AGN ($N_H > 10^{24}$ cm^{-2}). Then, we assume $L_{\mathrm{bol}}/L_{[\mathrm{Ne\,V}]} = (L_X/L_{[\mathrm{Ne\,V}]})_{\mathrm{type\,I}} \times (L_{\mathrm{bol}}/L_X) = 400 \times 20 = 8000$ for the bolometric correction. For [Ne V], we find $L_{\mathrm{bol}} \approx 1.3 \times 10^{45}$erg s^{-1} and $L_{\mathrm{bol}}/L_{\mathrm{Edd}} \approx 0.05$, using the SMBH–bulge mass relation of McConnell & Ma (2013) to estimate the SMBH mass and hence L_{Edd}. Similarly for [O III], we calculate $L_{\mathrm{bol,[O\,III]}} \approx 0.8$–$4.8 \times 10^{45}$erg s^{-1} and $L_{\mathrm{bol}}/L_{\mathrm{Edd}} \approx 0.05$–0.27 in the same manner as in the previous section for J1713+28. This bolometric Eddington fraction is about a factor of 2 larger than that found for J1713+28 (see Section 4.2.1), but the [O III] in both galaxies could be contaminated by star formation.

In fact, further inspection of J1506+54 reveals that its situation is even more unusual. Even for our sample of galaxies, this galaxy appears to have an unusually young ($\sim$3 Myr) and extreme ($\Sigma_{\mathrm{SFR}} \approx 3000$ M$_\odot$ yr^{-1} kpc^{-2}) stellar population. We, therefore, investigate the possibility that this galaxy has a starburst capable of exciting the [Ne V] line we observe. We compare this galaxy to blue compact dwarf galaxies, which can exhibit considerable [Ne V] emission without any other expected or conclusive signs of AGN activity (Izotov, Thuan & Privon 2012). For example, Izotov et al. (2004) found that $L_{[\mathrm{Ne\,V}]} \approx 7 \times 10^{38}$ erg s^{-1} for Tol 1214−27. To produce this emission, they calculated that $L_{>0.14\,\mathrm{keV}} \sim 10^{39-40}$ erg s^{-1} is required or about a factor of 10 higher than $L_{[\mathrm{Ne\,V}]}$. For J1506+54, we find $L_{[\mathrm{Ne\,V}]} = 1.5 \times 10^{40}$ erg s^{-1} and $L_X = 10^{41.9 \pm 1.0}$ erg s^{-1}. The X-ray luminosity likely suffers from Eddington bias (Eddington 1913). This arises because we sample counts from the Poisson distribution, which is especially asymmetric for low numbers of counts. A correction for this possible upward bias in this luminosity would only bring the X-ray luminosity more in line with the expected value based on the [Ne V] prediction. Therefore, it is plausible that all of the [Ne V] emission is produced by the very young, ultracompact starburst. This analysis emphasizes the overall conclusion in Section 4.2.1 that standard nebular diagnostics using high excitation lines as a tracer of AGN activity are frequently not useful diagnostics for these extreme galaxies.

While there is ambiguity about the origin of the [Ne V] in J1506+54, we can make the assumption that it traces obscured AGN activity and ask whether the AGN would be bolometrically dominant. Since both the AGN and starburst are heavily obscured, we consider their relative contributions to the 12 μm luminosity. We adopt $L_{12\,\mu\mathrm{m,AGN}} = L_{\mathrm{bol,\,AGN}}/9$ from Richards et al. (2006) and estimate $L_{12\,\mu\mathrm{m,AGN}} = 1.4 \times 10^{44}$ erg s^{-1} for J1506+54. Compared to the observed value (Table 4), this implies that roughly 11 per cent of the galaxy's MIR luminosity is powered by the AGN and $\sim$89 per cent is powered by star formation. This finding is consistent with the fact that starburst templates provide better fits to the IR SED than AGN templates (Diamond-Stanic et al. 2012).

4.2.3 X-ray diagnostics

X-ray observations are among the most efficient and unbiased ways of detecting and characterizing AGN (e.g. Mushotzky 2004). Here, we discuss the *Chandra* observations of the nine galaxies in our sample without an Mg II broad line. Our observations were designed to detect $10^{8.2-9.2}$ M$_\odot$ SMBHs radiating at $\sim$1 per cent of their Eddington limit with an obscuring column as high as $N_H = 10^{23}$ cm^{-2}. Based on the measured [O III] luminosities, we surmised that the galaxies were radiating at even higher rates, although as discussed in Section 4.2.1 some of the [O III] could come from star formation.

As described in Section 3.3, we detect only three of the nine narrow-line objects (J1506+54, J1613+28, and J2118+00) with *Chandra* with four counts each. We compare the [O III] and X-ray luminosities and upper limits in Fig. 6. The three detected narrow-line objects have large error bars, but are consistent with the relationship found for local type II AGN by Heckman et al. (2005).

However, in galaxies lacking powerful AGN, XRBs are responsible for the bulk of the 2–10 keV emission (e.g. Kong et al. 2003; Li et al. 2011). In star-forming galaxies, the emission is dominated by high-mass XRBs, which are associated with young (<100Myr) stellar populations. As a consequence, X-ray emission has been shown to scale with the SFR: $L_X \approx 3.5 \pm 0.4 \times 10^{39}$ erg s^{-1} per M$_\odot$ yr^{-1} (Grimm, Gilfanov & Sunyaev 2003; Mineo et al. 2014). Star formation in a merger event also produces measurable amounts of X-ray bright hot gas (Cox et al. 2006a), which has been shown to correlate with the SFR: $L_X \approx 8 \times 10^{38}$ erg s^{-1} per M$_\odot$ yr^{-1} (Owen & Warwick 2009; Mineo, Gilfanov & Sunyaev 2012).

[7] Photons with energies above 97 eV are required to create [Ne V], whereas stars typically do not produce photons beyond 54 eV (Abel & Satyapal 2008).

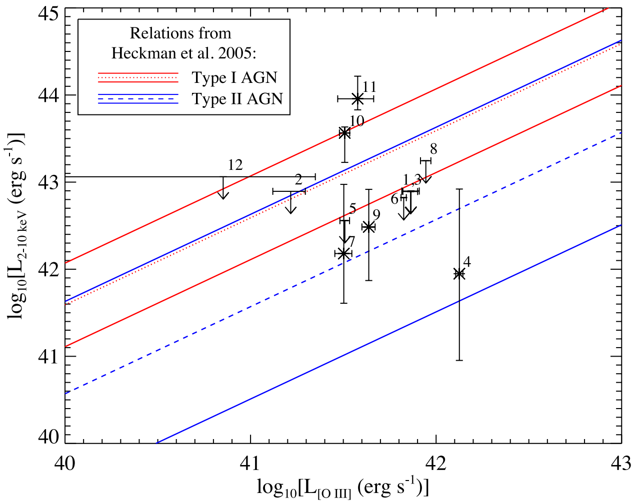

Figure 6. The X-ray luminosities and upper limits for our galaxies compared to the type I and type II AGN relations from Heckman et al. (2005). Note that the X-rays from all sources except J1359+51 and J1634+46 (IDs 10 and 11) are consistent with the level of X-rays from XRBs in these galaxies (see Section 4.2.3). Also, the [O III] emission from most of the sources is consistent with that from extreme starbursts (see Section 4.2.1).

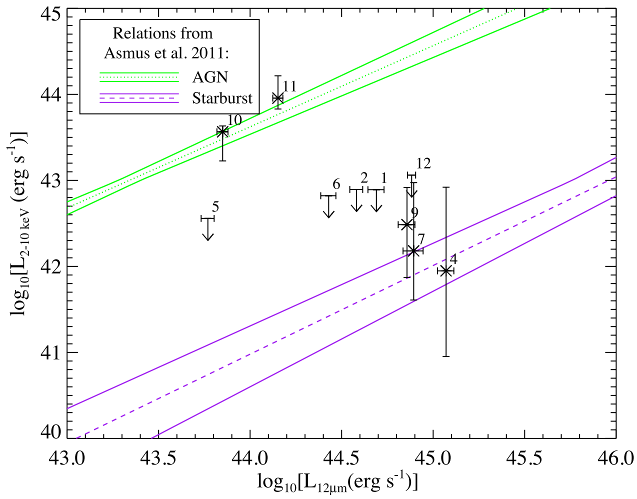

Figure 7. We compare our galaxies to the AGN and starburst relations from Asmus et al. (2011). The best-fitting and 1σ intervals for the relations are shown. The X-ray luminosities are not absorption corrected (see Section 4.2.3).

For the galaxies with 4-count X-ray detections (J1506+54, J1613+28, J2118+00), the IR-based SFRs from rest-frame *WISE* data are 250, 230, and 130 $\mathrm{M_{\odot}\ yr^{-1}}$ (see Table 4 and Section 3.5 for details). The predicted X-ray luminosities from star formation for these three galaxies are $\log(L_{\mathrm{X}}(\mathrm{erg\ s^{-1}})) = 41.9$, 41.9, and 41.6, respectively. Given that these numbers agree with the observations within the error bars and that the spectra are relatively soft (see Section 3.3), we conclude that the X-rays from all of the galaxies except the two type I AGN (J1359+51 and J1634+46) are likely from intense starbursts, not heavily obscured SMBHs.

4.2.4 IR diagnostics

To explore whether the narrow-line sources are Compton-thick AGN, we consider their IR luminosity. We derive rest-frame 12 μm luminosities from fits to the broad-band SED of the galaxies, which are constrained by *WISE* W3 and W4 in this spectral range. We also calculate the IRAC 3.6–4.5μm (Vega magnitudes) colours for our sources.

In Fig. 7, we plot the 2–10 keV luminosity versus the 12 μm luminosity of all the galaxies in our sample (narrow and broad line), with MIR photometry. Both luminosities are *K*-corrected. We do not correct the X-ray luminosities for absorption because we do not have enough information to do so, and fits to the X-ray spectra for the two type I AGN and the hardness ratio of the merged spectrum of the faint X-ray sources suggest only minor absorption. However, we do consider photon indices that encompass both obscured and unobscured AGN when we calculate the X-ray uncertainties (see Section 3.3). We overplot the relationship found by Asmus et al. (2011) for star-forming galaxies (purple) and absorption-corrected AGN (green).

As expected, the two X-ray-detected type I AGN (J1359+51 and J1634+46) lie near the AGN line. J2140+12 appears to be a considerably attenuated broad-line AGN based on differential attenuation of the optical and X-ray bolometric estimates and its position in Fig. 7, consistent with the suggestion in Section 4.1. The three X-ray-detected narrow-line sources are statistically consistent with the relation for starburst galaxies.

We also compare the available 3.6–4.5μm colour (in Vega magnitudes; see Table 4) for each source to the common colour cuts for MIR-selected AGN (see Mendez et al. 2013). We find 3.6–4.5μm colours of 0.18–0.61. The observed 5.8–8.0μm colour is unavailable in our *Spitzer* warm mission observations, but this does not significantly affect our comparison. The MIR colours of 4/7 of the narrow-line galaxies with IRAC data are relatively red (3.6–4.5μm ~ 0.6), consistent with the colours of AGN defined by Stern et al. (2005). However, they are in a region of colour space heavily contaminated by star-forming galaxies (Donley et al. 2012). None of the galaxies make new, higher fidelity AGN cut of 3.6–4.5 μm > 0.8 adopted by Stern et al. (2012). Therefore, there is no clear evidence for obscured AGN in this sample based on the available NIR colours. Overall, this IR analysis suggests that, even if Compton-thick AGN are present, they must not be a major contributor to the MIR luminosity. This is consistent with the finding for J1506+54 (Section 4.2.2).

5 DISCUSSION

5.1 Evidence for mergers

The $z = 0.4$–0.75 galaxies in our sample are unresolved in SDSS imaging. Our *HST*/WFC3 rest-frame *V*-band (∼550 nm) observations enable us to study their morphologies. Tidal tails and other debris indicative of a recent major or minor merger are evident in two-thirds of the sample (J0826+43, J1104+59, J1506+54, J1558+39, J1613+28, J1713+28, J2118+00, and J1634+46; see Figs 3 and 4 and Fig. A3 in the appendix). Our single-orbit images are fairly shallow, probing down to surface brightness levels of $\mu \sim 25$ mag arcsec^{-2}. Since tidal features are commonly at least one magnitude fainter than this (Duc & Renaud 2013), we cannot rule out their presence in the remaining three galaxies. 10 of the 12 galaxies have a single bright core, consistent with a late-stage merger where nuclear coalescence has already occurred, while 2 of the galaxies have another clearly associated, distinct, bright core within ∼20 kpc.

5.2 Extremely compact light profiles: evidence of unobscured AGN or compact starbursts?

One of the most significant and unexpected results of this work is the compact nature of the galaxy light profiles. Most of the objects in our sample have half-light radii less than a few hundred parsecs based on our Sérsic-only fits. The median value is $r_e = 251$ pc (using the brightest cores in the case of double nuclei). For comparison, a typical early-type galaxy at $z \sim 0.5$ has $r_e \sim 2000$ pc (e.g. Huertas-Company et al. 2013). We do not have sufficient data to correct our sizes for dust attenuation, but we estimate that such a correction would only make the r_e values smaller, depending on the magnitude of A_V (Arribas et al. 2012).

For many of the galaxies, our Sérsic + PSF fits suggest that a large fraction of the nuclear light (∼20–60 per cent) is unresolved. First, we consider if the source of this unresolved light for the three galaxies where we detect broad Mg II and Hβ emission lines (J1359+51, J1634+46, and J2140+12) is consistent with the amount of light expected for the broad-line AGN. We estimate the quasar contribution to the light in the WFC3/*F*814*W* filter by fitting galaxy and quasar templates to the UV–optical spectra (Section 3.1). Based on the spectra, we infer quasar light fractions of 31, 30, and 33 per cent in the *F*814*W* filter. The corresponding PSF light fractions measured from the *HST* data are 32, 17, and 50 per cent. The agreement is reasonable considering measurement uncertainties and the possibility of AGN variability in the ∼5 yr separating the acquisition of the spectra and images (e.g. Ulrich et al. 1997; McHardy 2013).

For the remaining nine galaxies, inspection of our UV–optical spectra show no evidence of a typical unobscured AGN (Fig. 2). In five of these galaxies (J0826+43, J0944+09, J1104+59, J1506+54, J1506+61), the PSF light fraction is substantial (40–60 per cent), and thus we would expect broad Mg II and Hβ emission lines to be visible if the PSF light were due to an unobscured AGN with a normal UV–optical spectrum. Fig. 8 illustrates this point for J1506+54.

However, the spectra do show an unexpected very blue continuum with weak nebular emission lines. We first investigate if the unresolved light could be consistent with weak emission-line quasars (WLQs; e.g. Diamond-Stanic et al. 2009; Plotkin et al. 2010). To compare our galaxies to WLQs, we calculate $\Delta\alpha_{ox}$, a diagnostic commonly used to compare WLQs to other similar populations of galaxies (e.g. BL Lacs). This quantity is defined as the X-ray brightness relative to typical radio-quiet quasars (for more details, see Wu et al. 2012). We compare our $\Delta\alpha_{ox}$ values to the 11 WLQs from Wu et al. (2012)[8] using the expectation from equation 3 of Just et al. (2007). In the astronomy survival statistical package (ASURV),[9] we use various two-sample statistical tests (Feigelson & Nelson 1985; Lavalley, Isobe & Feigelson 1992): Gehan's generalized Wilcoxon test (permutation and hypergeometric variances), logrank test, Peto and Peto generalized Wilcoxon test, and Peto and Prentice generalized Wilcoxon test. The probabilities that the samples are drawn from the same parent distribution are 0.2–0.5 per cent. Overall, this analysis leads us to conclude that it is unlikely that these spectra are consistent with WLQs.

The remaining likely explanations for the unresolved light in the *HST* images of the non-broad-line AGN are ultracompact starbursts. The presence of bolometrically weak, obscured AGN would not have a significant contribution to the optical continuum. Together, our emission-line, X-ray, and IR diagnostics (see Section 4) support this conclusion. In this case, there are a few possible explanations for the unusually blue continuum. One of the most plausible is very strong differential dust attenuation (i.e. the ionizing O stars are more heavily attenuated than the B stars). There is some evidence for this in two galaxies where it is possible to compare the nebular extinction using the Hγ and Hβ emission lines to the extinction to the galaxy's broad-band SED continuum. Other possibilities include leakage of ionizing continuum radiation or very abruptly truncated starbursts.

Therefore, we conclude that each of the PSF components in the galaxies that we have not classified as broad-line AGN are very compact stellar populations produced in central starbursts. When characterizing each galaxy light distribution, we do not wish to remove the central starburst; thus, we quote the half-light radius measured from the Sérsic fit rather than the Sérsic+PSF fit. While our sample is relatively small (12 galaxies), *HST* follow-up of an additional 17 galaxies has demonstrated that compactness is a near-ubiquitous property of our galaxies (Diamond-Stanic et al. 2012).

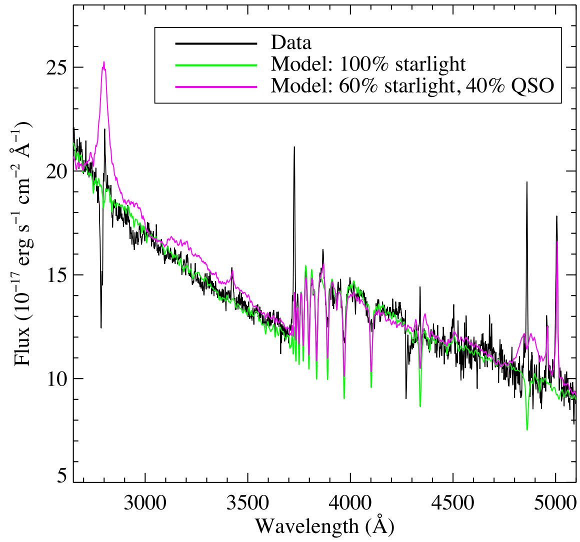

Figure 8. The black line shows the spectrum of J1506+54, a galaxy with an unresolved core that accounts for 47 per cent of the light in the rest-frame *g*-band *HST* image. The green line shows a stellar population model fit to the continuum. The magenta line shows a fit where a QSO template has been included. The QSO template accounts for 40 per cent of the light in the *g* band. The broad Mg II and Hβ emission lines are clearly visible in the template, but not in the data, ruling out the idea that the point source in the *HST* image is due to the presence of an unobscured AGN with a typical spectrum.

5.3 Comparison with theory

Numerical simulations suggest that compact central starbursts (0.01–1 kpc) are produced in dissipational (gas-rich) major mergers (Mihos & Hernquist 1994; Cox et al. 2006b; Hopkins et al. 2008b, 2009a). The remnants of such mergers are predicted to have two-component light profiles: an outer profile established by violent relaxation of stars present in the progenitors before final coalescence, and an inner stellar population formed from gas driven to the nuclear regions by strong tidal torques. A large fraction of local ellipticals appear to be consistent with this picture: their light profiles show central 'cusps' or light that is in excess of an inward extrapolation of an $r^{1/4}$ law fit to the outer regions (Kormendy et al.

[8] We only use these WLQs because they are at lower redshifts where the weak line is Mg II (as opposed to Lyα at $z > 2.2$) and because these WLQs are X-ray weak, more similar to our objects.

[9] http://astrostatistics.psu.edu/statcodes/sc_censor.html

2009, and references therein). Cusps with $r \lesssim 100$ pc have also been identified in NIR imaging of local ULIRGs and recent merger remnants (Rothberg & Joseph 2004; Haan et al. 2013). We hypothesize that the unresolved light in the galaxies not classified as broad-line AGN represents the central cusp predicted by simulations – i.e. stars formed from gas that sank to the inner regions of the potential well. At $z = 0.4$–0.75, the FWHM of the WFC3/$F814$ PSF is 400–540 pc, and thus it is unsurprising that we do not resolve these features.

Hopkins et al. (2008b) found that the mass fraction of the central starburst correlates with the initial gas fraction of the progenitor discs. Given our single-band *HST* imaging, we have not attempted to compute central starburst mass fractions. However, the light fraction represented by the PSF frac in Table 2 can provide a rough estimate of the mass fraction, given that much of the light in the outer dissipationless component comes from stars formed in the interaction but prior to nuclear coalescence. Indeed, 100 Myr after the final merger, Hopkins et al. (2008b) show that radial B-band mass-to-light variations are, at most, a factor of ∼2–3, with the inner regions sometimes having higher M_*/L_B due to dust attenuation.

Five of the nine narrow-line galaxies have PSF fractions in the range of 40–60 per cent, while the remaining four have PSF fractions less than 20 per cent. Notably, galaxies in this latter group show indications of having not reached complete nuclear coalescence including double nuclei (J1713+28), elliptical inner light profiles with large GALFIT residuals that may be consistent with dual nuclei slightly below the resolution limit (J1613+28 and J2118+00), and very bright inner tidal features (J1558+39, J1713+28, and J2118+00). If we assume that the 40–60 per cent PSF fractions of the more relaxed sources imply comparable central starburst mass fractions, the Hopkins simulations suggest that the progenitor discs must have had gas fractions in the range of 40–80 per cent. These gas fractions are at the upper end of the distribution for massive discs at $z \sim 0.5$ (Combes et al. 2013), consistent with the fact that our galaxies are very rare objects.

5.4 SMBH activity

It is widely believed that all massive galaxies with bulge-like cores contain SMBHs at their centres (e.g. Richstone et al. 1998). All of our galaxies are massive ($\log(M_*/\mathrm{M}_\odot) = 10.5$–$11.5$) and have centrally concentrated light distributions; thus, they are likely to host SMBHs. Recent theoretical work indicates that powerful AGN may be able to drive massive outflows from galaxies that quench star formation (e.g. King, Zubovas & Power 2011; Faucher-Giguère & Quataert 2012). Our goal is to determine what role, if any, SBMHs play in powering the galaxy-scale fast outflows that we observe in Mg II absorption in our galaxies. (The 12 galaxies in our sample were selected from a larger sample to be most-likely to host AGN activity; see Section 2 for details.) The first stage in this analysis is to determine the activity level of the SMBHs. We summarize our findings below.

3 of our 12 galaxies host broad-line AGN (see Section 4.1). Virial SMBH mass estimates suggest that they have masses of $\log(M_{\mathrm{SMBH}}/\mathrm{M}_\odot) = 8$–$9$ as expected. Two are X-ray detected and the third is undetected suggesting that it may be partially obscured. Estimates of the bolometric luminosity based on X-rays and the optical continuum suggest that the sources are radiating at ∼1–7 per cent of Eddington. Notably, in spite of the fairly high luminosity of the AGN, they provide only ∼30 per cent of the optical continuum. This is due to the fact that the massive host galaxy has very recently experienced a strong starburst.

The remaining nine galaxies exhibit narrow-line emission, but lack broad lines. For these galaxies, we consider the obscured AGN scenario, which is quite plausible for the narrow-line AGN given that (1) we know these are gas-rich, highly dissipative mergers where cold gas seems to be efficiently funnelled to the cores of the galaxies that have produced strong cusps and (2) broad-line AGN have been detected in three cases. A large accretion rate can produce a Compton-thick torus, where, in the unified AGN model (Urry & Padovani 1995), the inclination of the torus can strongly affect our ability to see the SMBH accretion disc. There is some evidence for large numbers of heavily obscured or Compton-thick nuclei in gas-rich galaxies (Daddi et al. 2007; Treister et al. 2010; Vignali et al. 2010; Fiore et al. 2012) that only very hard X-rays can pierce (Koss et al. 2011). However, we only find evidence for heavily obscured AGN in a small fraction of our sample, and our analysis presents a consistent picture that none of them are bolometrically dominant as compared to the compact central starbursts. We review these findings below.

We explored the narrow-line emission for the nine galaxies lacking broad lines to look for evidence of obscured AGN (see Section 4.2). We employed a variety of diagnostic diagrams designed to be similar to the classic BPT diagram (Fig. 5), but found that they produced inconsistent classifications both for our sample and a colour- and mass-matched comparison sample. Based on the strength of the high-excitation emission lines, [O III] and [Ne V], we consider the following three galaxies as candidate type II AGN: J1104+59 (ID 3), J1506+54 (ID 4), and J1713+28 (ID 8). Both J1104+59 and J1713+28 have high [O III]/Hβ ratios relative to our purely star-forming comparison sample (Fig. 5). However, the line ratios could still be consistent with star formation given the unusual physical conditions in the galaxies (Kewley et al. 2013a, 2013b). J1506+54 has a much lower [O III]/Hβ ratio but the highest [Ne V] luminosity of the sample (Table 5). [Ne V] has a very high ionization potential (97 eV) and is generally considered a good AGN indicator, but it is possible that the [Ne V] in J1506+54 is produced by the galaxy's hot young stars (Section 4.2.2). If we use the [Ne V] luminosity to estimate the AGN bolometric luminosity, we find $L_{\mathrm{bol}}/L_{\mathrm{Edd}} = 0.05$. Most importantly, we estimate that the AGN would produce only ∼10 per cent of the galaxy's MIR luminosity, with the remainder powered by the young starburst. Thus, while obscured AGN may be present in our sample, we conclude that they are not significant contributors to the galaxies' total luminosities.

Another possibility is that the combined duty cycle and Eddington ratios of these galaxies produce a population where less than half of the SMBHs have sufficiently high accretion rates to observe. This could arise because SMBHs experience state transitions similar to stellar mass BHs in XRBs, but on much longer time-scales given the large size scales involved (e.g. Merloni, Heinz & di Matteo 2003; Markoff et al. 2008). In uniformly selected samples of galaxies, it is not surprising to find a low active fraction of SMBHs represented by a duty cycle of ∼10–20 per cent (Fu et al. 2010; Diamond-Stanic et al. 2012). In fact, only ∼1 per cent of the galaxy population has $L/L_{\mathrm{Edd}} > 0.01$ (Aird et al. 2012). In addition, complete, distance-limited samples of galaxies probing SMBHs at X-ray wavelengths find that most galaxies have Eddington ratios $\lesssim 10^{-5}$ (Miller et al. 2012). Furthermore, only a fraction of SMBHs are radio-loud (e.g. Chen et al. 2013). This likely all arises from strong (factors of thousands to millions) AGN variability over long ($\gtrsim 10^4$ yr) time-scales that can only be constrained indirectly through observations of large populations of galaxies (Hickox et al. 2014). There is considerable evidence for this (e.g. AGN light echoes, the '*Fermi* bubbles'; e.g. Keel et al. 2012; Su & Finkbeiner 2012).

The fact that our galaxies appear to be late-stage mergers might suggest enhanced AGN activity. However, much is still unknown about how gas accretes on to the AGN from the galaxy. The theoretical work of Cen (2012) suggests that an SMBH does not enter a rapid accretion phase until ∼100 Myr after the starburst peak when the AGN can capture material from the slow winds of post-asymptotic giant branch stars. Most of our galaxies have ongoing star formation, and thus it may be that the SMBHs are not accreting at a high rate yet.

5.5 Is AGN feedback responsible for driving the galaxy-wide outflows and shutting off star formation in these galaxies?

A number of theoretical models have tried to link the SMBH to its larger scale surroundings. Wagner, Bicknell & Umemura (2012) suggest that feedback from AGN can be efficient in a clumpy, spherical medium if the AGN power is sufficiently close to $L_{\rm Edd}$. However, a key issue that is still not resolved is how AGN can inject considerable momentum to couple to a large fraction of the gas to drive it out of the galaxy (Debuhr, Quataert & Ma 2012). Wagner, Umemura & Bicknell (2013) suggest that this can be accomplished through ram pressure with dense clouds embedded in a tenuous, hot, hydrostatic medium. Alternatively, the potential for feedback may depend very strongly on the ability of outflowing energy from either starbursts or AGN to couple to dust (Novak, Ostriker & Ciotti 2012). AGN feedback is frequently modelled on small scales (e.g. Liu et al. 2013), which is difficult to causally connect to galaxy wide outflows.

Recent observational work has had a difficult time disentangling the effects of stars from the SMBH to resolve whether AGN or starburst feedback plays a more critical role in shutting off star formation and driving galactic-scale, fast outflows (Harrison et al. 2012). There is considerable observational evidence for dominant AGN feedback on small scales, where it can be better separated from starburst feedback: NGC 1266 (Alatalo et al. 2013), Mrk 231 (Feruglio et al. 2010). However, whether the SMBH is primarily responsible for driving the galaxy-wide outflows in star-forming galaxies has not been fully resolved. In fact, when the SMBH injects energy into the surrounding gas, it is not clear if it has a net negative or positive effect on these galaxies. In some situations, the SMBH can actually help to trigger a starburst (e.g. Zubovas et al. 2013).

In a companion paper, Diamond-Stanic et al. (2012) analysed 29 galaxies (of which our 12 galaxies are a subsample) drawn from our larger galaxy sample. Their analysis combined the available broad-band SEDs compared to a few starburst and quasar models, the compactness of the galaxies deduced from *HST* observations, highly blueshifted absorption lines indicative of massive outflows, and model comparisons to the estimated SFR surface density. They concluded that AGN feedback is not *required* by arguing that compact starbursts are capable of driving massive, galaxy-wide outflows at ∼1000 km s^{-1}. We revisit this issue here in a more detailed presentation of our multiwavelength data including critical, new information on the AGN content for our subsample.

We detect high-velocity outflows based on Mg II absorption line measurements in 9/12 galaxies in our sample. Of the three galaxies hosting broad-line AGN, only J2140+12 shows Mg II absorption. We hypothesize that outflows may be present in the other two broad-line AGN but the magnesium in the outflow may exist in a higher ionization stage due to exposure to the AGN's hard photoionizing continuum (Hennawi & Prochaska 2013). Notably, J2140+12 is not detected in the X-rays suggesting partial obscuration of the nuclear source, which may explain why Mg II is present in absorption (see Section 4.1). The outflow velocity measured for J2140+12 is the second slowest in our sample.

Of the nine narrow-line galaxies, eight have outflows based on highly blueshifted Mg II absorption. We have found evidence for type II AGN in only three galaxies (J1104+59, J1506+54, and J1713+28), but the results are somewhat ambiguous (see Section 5.4 for a discussion); these galaxies have a range of outflow velocities consistent with the rest of the narrow-line galaxies. As noted previously, we cannot conclusively rule out the presence of a Compton-thick AGN in any of these narrow-line galaxies.

Fig. 9 best summarizes our findings. We plot the maximum outflow velocity as a function of the galaxy half-light radius and [Ne V] luminosity to explore whether the outflow velocity is more closely related to galaxy morphology or nuclear activity. We find that all of the galaxies with the fastest outflows (<-1000 km s^{-1}) are compact starbursts ($r_{\rm e} < 1$ kpc). The median half-light radius of these galaxies is $r_{\rm e} = 251$ pc. Three of the seven galaxies with $v_{\rm max} < -1000$ km s^{-1} have some evidence for obscured AGN activity, but the highest velocity outflow ($v_{\rm max} = -2440$ km s^{-1}) is found in a galaxy with no evidence for AGN activity (J1613+28). Only one of the three unequivocal (broad-line) AGN has a detected outflow (J2140+12); this galaxy has one of the slowest outflows in the sample ($v_{\rm avg} = -490$ km s^{-1}, $v_{\rm max} = -950$ km s^{-1}). We also find that [Ne V], which is a common tracer of AGN activity given the high excitation energies required, shows no correlation with outflow velocity, as would be expected if AGN were driving the outflows. If we plot the [Ne V] bolometric Eddington fraction, we find similar results. Furthermore, the possible obscured AGN in the galaxy with the highest [Ne V] luminosity (J1506+54) accounts for only ∼11 per cent of the galaxy's MIR luminosity, suggesting that obscured star formation dominates the galaxy's bolometric luminosity. Therefore, we conclude that the presence of a powerful outflow seems to be more closely linked to the star formation properties of the host galaxies rather than the AGN. This is reminiscent of fig. 4 of Diamond-Stanic et al. (2012), who showed that the outflow is linked with the SFR surface density.

Despite the apparent lack of correlation between the high outflow velocities and AGN activity in this sample, it remains possible that the outflows were driven in the recent past by AGN activity that has since switched off and is no longer visible. A strong correlation has recently been observed between nuclear star formation and AGN activity (e.g. Diamond-Stanic & Rieke 2012; Esquej et al. 2013), suggesting that our sources, which exhibit strong nuclear starbursts, may be more likely to host a powerful AGN. If the AGN experiences rapid variability over a large dynamic range of several orders of magnitude (see Hickox et al. 2014, for a discussion), the possibility exists that a wind could have been launched by an AGN that has rapidly decreased in luminosity, while the outflow persists over longer time-scales (Zubovas & King 2014). This scenario cannot be conclusively ruled out from our observations; however, the ubiquity of rapid outflows among our sample would suggest that essentially all our galaxies have hosted an AGN in the recent past, which imply a remarkably strong connection between nuclear star formation and AGN activity. Given that the highly compact starbursts themselves may be capable of producing the high-velocity winds (e.g. Heckman et al. 2011), a more straightforward explanation is that AGN driving is simply not required, and this is the interpretation that we favour here.

The additional lack of bright radio emission in these galaxies suggests that radio jets do not play a major role, at least shortly after the merger, but that the powerful, compact starburst initially drives out the gas in a galaxy-wide outflow. While considerable

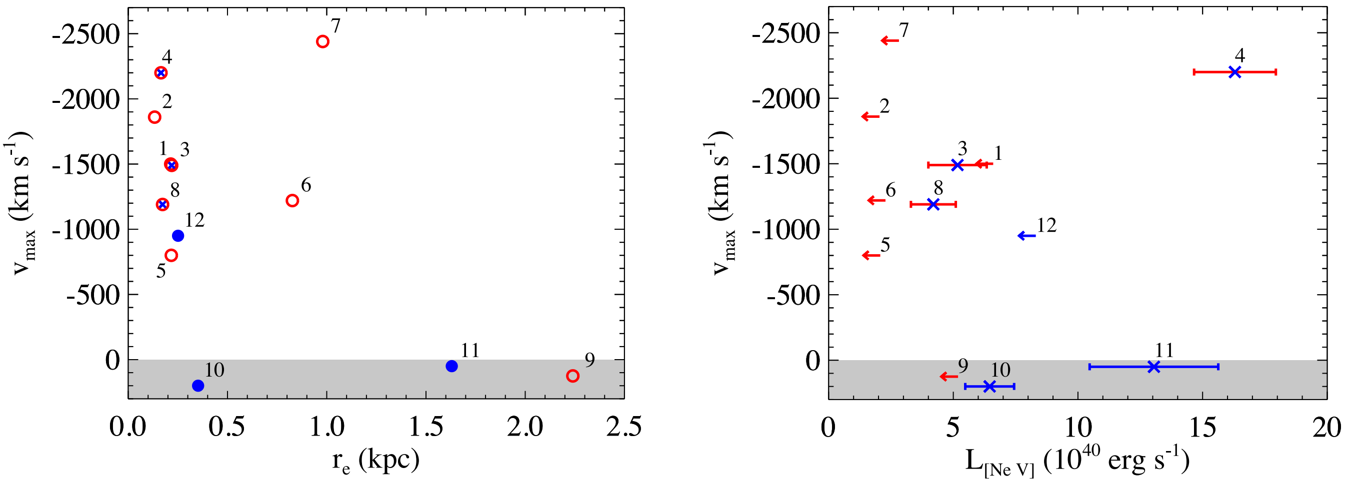

Figure 9. These plots bring together our spectroscopic, AGN, and morphological analysis to examine the correlation or lack thereof between outflow velocities, size, and AGN content. The colours in both plots highlight the different source classifications: blue for AGN and red for starbursts. Blue-only points (filled circles on the left) have broad-line AGN; red-only points (open circles on the left) are consistent with pure star formation; points with a combination of blue and red (with 'X's' on the left) indicate emission lines consistent with extreme star formation and type II AGN (ambiguous). In both parts of the figure, we plot the maximum outflow velocity (the trends are the same when using the average velocity, as the two velocities are highly correlated – see Section 3.1). In 3/12 cases where no outflow is detected, we assigned slightly different positive velocities for clarity only. On the left, we plot the outflow velocity as a function of the best-fitting single Sérsic model effective radius (a measure of compactness; where there are two cores, we use the radius of the brighter one). On the right, we plot the outflow velocity as a function of the [Ne v] luminosity (high-excitation [Ne v] is generally a good tracer of AGN activity but see Section 4.2.2 for caveats). If [Ne v] is tracing AGN activity and the AGN drive the outflows, we would expect to see a correlation, but we do not. These plots support our conclusion that the galaxy-wide outflows appear to be driven by extreme starbursts, not AGN.

non-luminous, mechanical energy is contained in SMBH jets and disc winds, which could be larger during low-luminosity states (e.g. Heinz, Merloni & Schwab 2007; Körding et al. 2008), the relative efficiency of SMBH mechanical energy is typically modelled to be approximately two orders of magnitude below that of radiation pressure feedback for PSBGs (e.g. Ciotti, Ostriker & Proga 2010). Furthermore, Karouzos et al. (2014) find that radio jets can suppress star formation in their host galaxies but appear not to totally quench it.

These findings together generally support the major merger evolutionary scenario first developed by Sanders et al. (1988), where a gas-rich merger produces a shrouded, dusty starburst. Then after some time, the SMBH is uncovered as the remnant ages to become an early-type galaxy. This scenario is also consistent with more recent models where the AGN is efficiently fuelled *after* the starburst has ended (e.g. Cen 2012). Later, the SMBH launches powerful radio jets from the centre of an elliptical remnant into a hot, tenuous ISM, which can act to maintain the state of the gas as a low-excitation radio AGN (e.g. Smolčić et al. 2009).

Our results agree with the primary result of Diamond-Stanic et al. (2012) that the $v \propto r^{-1/2}$ scaling for winds driven by either supernovae or radiation pressure from massive stars can drive outflows up to the extreme velocities we observe. Furthermore, we find that the presence of an AGN does not imply a higher outflow velocity. This is consistent with the results of Coil et al. (2011) who explored outflows in samples of X-ray-selected AGN and classic post-starburst (K+A) galaxies at intermediate redshifts and found $v \sim -200$ km s^{-1}, irrespective of nuclear activity. Given the low inferred contributions of the AGN to the galaxies' bolometric luminosities and the lack of conclusive AGN activity in the galaxies with the fastest outflows, we conclude that AGN feedback does not appear to be the dominant mode of feedback for these galaxies. Altogether, this discussion suggests that the galaxy-wide outflows in this sample of galaxies are primarily driven by extreme starbursts.

6 SUMMARY AND CONCLUSIONS

We have analysed *HST* and *Chandra* images, UV–optical spectra, UV–MIR photometric data, and JVLA radio data on a subsample of massive galaxies at $z = 0.4$–0.75 in the midst of star formation quenching. These galaxies were selected from a larger parent sample as the most likely to host AGN. Our primary goal is to understand the activity of their SMBHs and the morphology of their host galaxies to gain insight into whether the SMBHs drove the galaxy-wide outflows and played the primary role in shutting down their recent star formation. A summary of our findings is presented below.

(i) Rest-frame *V*-band *HST* imaging reveals tidal tails or disturbed morphologies indicative of a recent major or minor merger in 9/12 galaxies. Given the shallow depth of our images, we cannot rule out the presence of such features in the remaining galaxies. We conclude that the recent starburst in all of our galaxies was likely triggered by a merger.

(ii) All of the galaxies have very compact light profiles. J1558+39, J1613+28, J1713+28, and J2118+00 appear to be in the midst of nuclear coalescence and have not relaxed yet. Excluding these galaxies and the three type I AGN, we measure effective radii of 0.1–0.2 kpc using a single Sérsic fit. These objects are better fitted by a combination of a Sérsic profile and a nuclear point source which contains 40–60 per cent of the total light. We argue that the unresolved light is not due to an AGN because we see no evidence of broad Mg II or Hβ emission lines in the optical spectrum and the probability that these galaxies are consistent with weak-lined AGN is small based on their α_{ox} ratios. We conclude that the nuclear light is likely due to a compact (<0.5 kpc) central starburst triggered by the dissipative collapse of very gas rich progenitor discs, as suggested by theoretical models (cf. Hopkins et al. 2009a).

(iii) Three of the galaxies (J1359+51, J1634+46, and J2140+12) are broad-line AGN. We use the width of the broad Mg II emission lines to derive virial masses of $M_{SMBH} \sim 10^8$–10^9 M$_\odot$.

Two of the AGN are X-ray detected (J1359+51 and J1634+46) and one is radio-loud (J1634+46). We calculate that they are radiating at ∼1–7 per cent of their Eddington luminosities.

(iv) Based on high-excitation emission-line diagnostics, only 3/9 narrow-line galaxies (J1104+59, J1506+54, and J1713+28) exhibit signs of obscured AGN. The bolometric Eddington fractions are similar to those found for the broad-line AGN, but even more uncertain because the emission is also consistent with the presence of an ultracompact starburst; this leads to somewhat ambiguous results. In one case, J1506+54, we find that only 11 per cent of the MIR luminosity is due to the AGN with the remainder coming from star formation.

(v) The other six galaxies in the sample are completely consistent with compact starbursts. We have shown that analysis of BPT-type diagrams does not provide a clear indication of AGN activity for these galaxies primarily because the [O III]/Hβ ratio does not discriminate extreme starbursts well. In addition, although faint levels of X-ray emission are observed in three of these galaxies, the derived X-ray luminosities and stacked hardness ratio are entirely consistent with emission from XRBs given the large recent SFRs of these galaxies. While we cannot conclusively rule out Compton-thick AGN in these sources, we suggest that star formation is likely to be the dominant contributor to the galaxies' bolometric luminosities.

(vi) Nine of our galaxies show evidence of ultrafast ($v_{\rm max} \gtrsim 1000$ km s^{-1}) Mg II outflows. Only one of the three unequivocally identified (broad-line) AGN has a detected outflow, and it is the slowest or second slowest in the sample, depending on how the outflow velocity is measured. The light from 5/9 of the galaxies with the ultrafast outflows is completely consistent with compact starbursts (and in 3/9 cases, we are unable to conclusively differentiate between starburst and AGN activity). We conclude that outflow properties are not linked to ongoing AGN activity.

These results support the primary conclusion of Diamond-Stanic et al. (2012), who argued that our ultracompact galaxies have the physical conditions necessary to launch the high-velocity outflows we observe by highlighting the $v \propto r^{-1/2}$ scaling for winds driven by either supernovae or radiation pressure from massive stars. To this argument, we add the fact that the presence of a luminous AGN does not appear to have any positive correlation with Mg II absorption strength or outflow velocity. This study and Diamond-Stanic et al. (2012) cannot and did not conclusively rule out that AGN play at least a minor role at some point in the evolution of these galaxies. However, we do not find any evidence directly in support of AGN feedback in this sample of galaxies, and AGN feedback is unnecessary to explain the observations. Overall, we conclude that these galaxies are massive merger remnants with high-velocity outflows primarily driven by powerful, unusually compact starbursts.

ACKNOWLEDGEMENTS

Support for this work was provided by the National Aeronautics and Space Administration (NASA) through *Chandra* award number GO0-11135A issued by the *Chandra X-ray Observatory* Center, which is operated by the Smithsonian Astrophysical Observatory (SAO) for and on behalf of the NASA under contract NAS8-03060. Support was also provided by *HST* programmes HST-G0-12019 and HST-GO-12272, which were funded by NASA through a grant from the Space Telescope Science Institute (STScI), which is operated by the Association of Universities for Research in Astronomy (AURA), Incorporated, under NASA contract NAS5-26555. This work is based in part on observations made with the *Spitzer Space Telescope* (Spitzer-GO-60145), which is operated by the Jet Propulsion Laboratory (JPL), California Institute of Technology under a contract with NASA. Support for this work was also provided by NASA through an award issued by JPL/Caltech. AD-S acknowledges support from The Grainger Foundation and from the Southern California Center for Galaxy Evolution, a multicampus research programme funded by the University of California Office of Research. AC acknowledges support from NSF CAREER award AST-1055081. CT and GR acknowledge the support of the Alexander von Humboldt Foundation.

REFERENCES

Abazajian K. N. et al., 2009, ApJS, 182, 543
Abel N. P., Satyapal S., 2008, ApJ, 678, 686
Adelman-McCarthy J. K. et al., 2006, ApJS, 162, 38
Aihara H. et al., 2011, ApJS, 193, 29
Aird J. et al., 2012, ApJ, 746, 90
Alatalo K. et al., 2013, in Zhang C. M., Belloni T., Méndez M., Zhang S. N., eds, Proc. IAU Symp. 290, Feeding Compact Objects: Accretion on All Scales. Cambridge Univ. Press, Cambridge, p. 175
Arribas S., Colina L., Alonso-Herrero A., Rosales-Ortega F. F., Monreal-Ibero A., García-Marín M., García-Burillo S., Rodríguez-Zaurín J., 2012, A&A, 541, A20
Asmus D., Gandhi P., Smette A., Hönig S. F., Duschl W. J., 2011, A&A, 536, A36
Avni Y., 1976, ApJ, 210, 642
Baldwin J. A., Phillips M. M., Terlevich R., 1981, PASP, 93, 5
Barro G. et al., 2013, ApJ, 765, 104
Becker R. H., White R. L., Helfand D. J., 1995, ApJ, 450, 559
Behroozi P. S., Wechsler R. H., Conroy C., 2013, ApJ, 770, 57
Bertin E., Arnouts S., 1996, A&AS, 117, 393
Booth C. M., Schaye J., 2013, Nature Scientific Reports, 1738, available at: http://www.nature.com/srep/2013/130515/srep01738/full/srep01738.html
Brightman M. et al., 2013, MNRAS, 433, 2485
Brinchmann J., Pettini M., Charlot S., 2008, MNRAS, 385, 769
Broos P. S., Townsley L. K., Feigelson E. D., Getman K. V., Bauer F. E., Garmire G. P., 2010, ApJ, 714, 1582
Bruzual A. G., 2007, in Vazdekis A., Peletier R. F., eds, Proc. IAU Symp. 241, Stellar Populations as Building Blocks of Galaxies. Cambridge Univ. Press, Cambridge, p. 125
Bruzual G., Charlot S., 2003, MNRAS, 344, 1000
Buitrago F., Trujillo I., Conselice C. J., Bouwens R. J., Dickinson M., Yan H., 2008, ApJ, 687, L61
Canalizo G., Bennert N., Jungwiert B., Stockton A., Schweizer F., Lacy M., Peng C., 2007, ApJ, 669, 801
Cano-Díaz M., Maiolino R., Marconi A., Netzer H., Shemmer O., Cresci G., 2012, A&A, 537, L8
Cash W., 1979, ApJ, 228, 939
Cassata P. et al., 2011, ApJ, 743, 96
Cen R., 2012, ApJ, 755, 28
Chabrier G., 2003, PASP, 115, 763
Charlot S., Fall S. M., 2000, ApJ, 539, 718
Chary R., Elbaz D., 2001, ApJ, 556, 562
Chen Y.-M. et al., 2013, MNRAS, 429, 2643
Ciotti L., Ostriker J. P., Proga D., 2010, ApJ, 717, 708
Coil A. L., Weiner B. J., Holz D. E., Cooper M. C., Yan R., Aird J., 2011, ApJ, 743, 46
Combes F., García-Burillo S., Braine J., Schinnerer E., Walter F., Colina L., 2013, A&A, 550, A41
Covington M. D., Primack J. R., Porter L. A., Croton D. J., Somerville R. S., Dekel A., 2011, MNRAS, 415, 3135
Cox T. J., Di Matteo T., Hernquist L., Hopkins P. F., Robertson B., Springel V., 2006a, ApJ, 643, 692

Cox T. J., Dutta S. N., Di Matteo T., Hernquist L., Hopkins P. F., Robertson B., Springel V., 2006b, ApJ, 650, 791
Croton D. J. et al., 2006, MNRAS, 365, 11
Daddi E. et al., 2007, ApJ, 670, 173
Dale D. A. et al., 2005, ApJ, 633, 857
Debuhr J., Quataert E., Ma C.-P., 2012, MNRAS, 420, 2221
Diamond-Stanic A. M., Rieke G. H., 2012, ApJ, 746, 168
Diamond-Stanic A. M. et al., 2009, ApJ, 699, 782
Diamond-Stanic A. M., Moustakas J., Tremonti C. A., Coil A. L., Hickox R. C., Robaina A. R., Rudnick G. H., Sell P. H., 2012, ApJ, 755, L26
Dickey J. M., Lockman F. J., 1990, ARA&A, 28, 215
Donley J. L. et al., 2012, ApJ, 748, 142
Dopita M. A. et al., 2005, ApJ, 619, 755
Dopita M. A. et al., 2006a, ApJS, 167, 177
Dopita M. A. et al., 2006b, ApJ, 647, 244
Dressler A., Gunn J. E., 1983, ApJ, 270, 7
Duc P.-A., Renaud F., 2013, in Souchay J., Mathis S., Tokieda T., eds, Lecture Notes in Physics, Vol. 861, Tides in Astronomy and Astrophysics. Springer-Verlag, Berlin, p. 327
Eddington A. S., 1913, MNRAS, 73, 359
Erb D. K., Shapley A. E., Pettini M., Steidel C. C., Reddy N. A., Adelberger K. L., 2006, ApJ, 644, 813
Esquej P. et al., 2013, A&A, 557, A123
Fan L., Fang G., Chen Y., Pan Z., Lv X., Li J., Lin L., Kong X., 2013, ApJ, 771, L40
Faucher-Giguère C.-A., Quataert E., 2012, MNRAS, 425, 605
Fazio G. G. et al., 2004, ApJS, 154, 10
Feigelson E. D., Nelson P. I., 1985, ApJ, 293, 192
Ferland G. J., Osterbrock D. E., 1986, ApJ, 300, 658
Feruglio C., Maiolino R., Piconcelli E., Menci N., Aussel H., Lamastra A., Fiore F., 2010, A&A, 518, L155
Fiore F. et al., 2012, A&A, 537, A16
Freeman P., Doe S., Siemiginowska A., 2001, in Starck J.-L., Murtagh F. D., eds, Proc. SPIE Conf. Ser. Vol. 4477, Astronomical Data Analysis. SPIE, Bellingham, p. 76
Fruscione A. et al., 2006, in Silva D. R., Doxsey R. E., eds, Proc. SPIE Conf. Ser. Vol. 6270, Observatory Operations: Strategies, Processes, and Systems. SPIE, Bellingham, p. 62701V
Fu H. et al., 2010, ApJ, 722, 653
Gabor J. M., Davé R., Oppenheimer B. D., Finlator K., 2011, MNRAS, 417, 2676
Garmire G. P., Bautz M. W., Ford P. G., Nousek J. A., Ricker G. R., Jr, 2003, in Truemper J. E., Tananbaum H. D., eds, Proc. SPIE Conf. Ser. Vol. 4851, X-Ray and Gamma-Ray Telescopes and Instruments for Astronomy. SPIE, Bellingham, p. 28
Geach J. E. et al., 2013, ApJ, 767, L17
Gilli R., Vignali C., Mignoli M., Iwasawa K., Comastri A., Zamorani G., 2010, A&A, 519, A92
Granato G. L., De Zotti G., Silva L., Bressan A., Danese L., 2004, ApJ, 600, 580
Greene J. E., Zakamska N. L., Ho L. C., Barth A. J., 2011, ApJ, 732, 9
Greene J. E., Zakamska N. L., Smith P. S., 2012, ApJ, 746, 86
Grimm H., Gilfanov M., Sunyaev R., 2003, MNRAS, 339, 793
Groves B., Dopita M. A., Sutherland R. S., Kewley L. J., Fischera J., Leitherer C., Brandl B., van Breugel W., 2008, ApJS, 176, 438
Haan S. et al., 2013, MNRAS, 434, 1264
Hainline K. N., Hickox R., Greene J. E., Myers A. D., Zakamska N. L., 2013, ApJ, 774, 145
Harrison C. M. et al., 2012, MNRAS, 426, 1073
Heckman T. M., Kauffmann G., Brinchmann J., Charlot S., Tremonti C., White S. D. M., 2004, ApJ, 613, 109
Heckman T. M., Ptak A., Hornschemeier A., Kauffmann G., 2005, ApJ, 634, 161
Heckman T. M. et al., 2011, ApJ, 730, 5
Heinz S., Merloni A., Schwab J., 2007, ApJ, 658, L9
Hennawi J. F., Prochaska J. X., 2013, ApJ, 766, 58
Hickox R. C., Mullaney J. R., Alexander D. M., Chen C.-T. J., Civano F. M., Goulding A. D., Hainline K. N., 2014, ApJ, 782, 9
Hook R., Stoehr F., 2008, Technical report, WFC3 Support in Tiny Tim
Hopkins P. F., Hernquist L., Cox T. J., Di Matteo T., Robertson B., Springel V., 2006, ApJS, 163, 1
Hopkins P. F., Cox T. J., Kereš D., Hernquist L., 2008a, ApJS, 175, 390
Hopkins P. F., Hernquist L., Cox T. J., Dutta S. N., Rothberg B., 2008b, ApJ, 679, 156
Hopkins P. F., Cox T. J., Dutta S. N., Hernquist L., Kormendy J., Lauer T. R., 2009a, ApJS, 181, 135
Hopkins P. F., Bundy K., Murray N., Quataert E., Lauer T. R., Ma C.-P., 2009b, MNRAS, 398, 898
Huertas-Company M. et al., 2013, MNRAS, 428, 1715
Izotov Y. I., Noeske K. G., Guseva N. G., Papaderos P., Thuan T. X., Fricke K. J., 2004, A&A, 415, L27
Izotov Y. I., Thuan T. X., Privon G., 2012, MNRAS, 427, 1229
Jedrzejewski R., Hack W., Hanley C., Busko I., Koekemoer A. M., 2005, in Shopbell P., Britton M., Ebert R., eds, ASP Conf. Ser. Vol. 347, Astronomical Data Analysis Software and Systems XIV. Astron. Soc. Pac., San Francisco, p. 129
Juneau S., Dickinson M., Alexander D. M., Salim S., 2011, ApJ, 736, 104
Just D. W., Brandt W. N., Shemmer O., Steffen A. T., Schneider D. P., Chartas G., Garmire G. P., 2007, ApJ, 665, 1004
Karouzos M. et al., 2014, ApJ, 784, 137
Kauffmann G., Heckman T. M., 2009, MNRAS, 397, 135
Kauffmann G. et al., 2003, MNRAS, 346, 1055
Keel W. C. et al., 2012, MNRAS, 420, 878
Kelly B. C., Shen Y., 2013, ApJ, 764, 45
Kelly B. C., Vestergaard M., Fan X., Hopkins P., Hernquist L., Siemiginowska A., 2010, ApJ, 719, 1315
Kennicutt R. C., Jr, 1998, ApJ, 498, 541
Kereš D., Katz N., Davé R., Fardal M., Weinberg D. H., 2009, MNRAS, 396, 2332
Kewley L. J., Dopita M. A., Sutherland R. S., Heisler C. A., Trevena J., 2001, ApJ, 556, 121
Kewley L. J., Groves B., Kauffmann G., Heckman T., 2006, MNRAS, 372, 961
Kewley L. J., Maier C., Yabe K., Ohta K., Akiyama M., Dopita M. A., Yuan T., 2013a, ApJ, 774, L10
Kewley L. J., Dopita M. A., Leitherer C., Dave R., Yuan T., Allen M., Groves B., Sutherland R., 2013b, ApJ, 774, 100
Kimble R. A., MacKenty J. W., O'Connell R. W., Townsend J. A., 2008, in Oschmann J. M., Jr, de Graauw M. W. M., MacEwen H. A., eds, Proc. SPIE Conf. Ser. Vol. 7010, Space Telescopes and Instrumentation 2008: Optical, Infrared, and Millimeter. SPIE, Bellingham, p. 70101E
King A. R., Zubovas K., Power C., 2011, MNRAS, 415, L6
Kolmogorov A., 1941, Ann. Math. Stat., 12, 461
Kong A. K. H., DiStefano R., Garcia M. R., Greiner J., 2003, ApJ, 585, 298
Körding E., Rupen M., Knigge C., Fender R., Dhawan V., Templeton M., Muxlow T., 2008, Science, 320, 1318
Kormendy J., Fisher D. B., Cornell M. E., Bender R., 2009, ApJS, 182, 216
Koss M., Mushotzky R., Veilleux S., Winter L. M., Baumgartner W., Tueller J., Gehrels N., Valencic L., 2011, ApJ, 739, 57
Lamareille F., 2010, A&A, 509, A53
Lavalley M., Isobe T., Feigelson E., 1992, in Worrall D. M., Biemesderfer C., Barnes J., eds, ASP Conf. Ser. Vol. 25, Astronomical Data Analysis Software and Systems I. Astron. Soc. Pac., San Francisco, p. 245
Lee J.-S., 1986, Opt. Eng., 25, 636
Lehnert M. D., Heckman T. M., 1996, ApJ, 472, 546
Li Z., Garcia M. R., Forman W. R., Jones C., Kraft R. P., Lal D. V., Murray S. S., Wang Q. D., 2011, ApJ, 728, L10
Lipari S. et al., 2009, MNRAS, 392, 1295
Liu X., Shapley A. E., Coil A. L., Brinchmann J., Ma C.-P., 2008, ApJ, 678, 758
Liu C., Yuan F., Ostriker J. P., Gan Z., Yang X., 2013, MNRAS, 434, 1721
Lupie O., Boucarut R., 2003, Technical report, WFC3 UVIS Filters: Measured Throughput and Comparison to Specifications
Maiolino R., Risaliti G., 2007, in Ho L. C., Wang J.-W., eds, ASP Conf. Ser. Vol. 373, The Central Engine of Active Galactic Nuclei. Astron. Soc. Pac., San Francisco, p. 447

Marconi A., Hunt L. K., 2003, ApJ, 589, L21
Markoff S. et al., 2008, ApJ, 681, 905
Martin C. L., 2005, ApJ, 621, 227
Martin D. C. et al., 2005, ApJ, 619, L1
McConnell N. J., Ma C.-P., 2013, ApJ, 764, 184
McHardy I. M., 2013, MNRAS, 430, L49
Menci N., Fontana A., Giallongo E., Grazian A., Salimbeni S., 2006, ApJ, 647, 753
Mendez A. J. et al., 2013, ApJ, 770, 40
Merloni A., Heinz S., Di Matteo T., 2003, MNRAS, 345, 1057
Meurer G. R., Heckman T. M., Lehnert M. D., Leitherer C., Lowenthal J., 1997, AJ, 114, 54
Mihos J. C., Hernquist L., 1994, ApJ, 437, L47
Miller J. M., Pooley G. G., Fabian A. C., Nowak M. A., Reis R. C., Cackett E. M., Pottschmidt K., Wilms J., 2012, ApJ, 757, 11
Mineo S., Gilfanov M., Sunyaev R., 2012, MNRAS, 426, 1870
Mineo S., Gilfanov M., Lehmer B. D., Morrison G. E., Sunyaev R., 2014, MNRAS, 437, 1698
Morrison J. E., Röser S., McLean B., Bucciarelli B., Lasker B., 2001, AJ, 121, 1752
Moustakas J., Kennicutt R. C., Jr, 2006, ApJS, 164, 81
Moustakas J. et al., 2013, ApJ, 767, 50
Murray N., Quataert E., Thompson T. A., 2005, ApJ, 618, 569
Mushotzky R., 2004, in Barger A. J., ed., Astrophysics and Space Science Library, Vol. 308, Supermassive Black Holes in the Distant Universe. Kluwer, Dordrecht, p. 53
Nielsen D. M., Ridgway S. E., De Propris R., Goto T., 2012, ApJ, 761, L16
Nousek J. A., Shue D. R., 1989, ApJ, 342, 1207
Novak G. S., Ostriker J. P., Ciotti L., 2012, MNRAS, 427, 2734
Owen R. A., Warwick R. S., 2009, MNRAS, 394, 1741
Page K. L., Reeves J. N., O'Brien P. T., Turner M. J. L., 2005, MNRAS, 364, 195
Park T., Kashyap V. L., Siemiginowska A., van Dyk D. A., Zezas A., Heinke C., Wargelin B. J., 2006, ApJ, 652, 610
Patel S. G., Holden B. P., Kelson D. D., Franx M., van der Wel A., Illingworth G. D., 2012, ApJ, 748, L27
Peng C. Y., Ho L. C., Impey C. D., Rix H.-W., 2002, AJ, 124, 266
Peng C. Y., Ho L. C., Impey C. D., Rix H., 2010, AJ, 139, 2097
Petry D. CASA Development Team, 2012, in Ballester P., Egret D., Lorente N. P. F., eds, ASP Conf. Ser. Vol. 461, Astronomical Data Analysis Software and Systems XXI. Astron. Soc. Pac., San Francisco, p. 849
Plotkin R. M., Anderson S. F., Brandt W. N., Diamond-Stanic A. M., Fan X., MacLeod C. L., Schneider D. P., Shemmer O., 2010, ApJ, 721, 562
Poggianti B. M., Smail I., Dressler A., Couch W. J., Barger A. J., Butcher H., Ellis R. S., Oemler A., Jr, 1999, ApJ, 518, 576
Rich J. A., Kewley L. J., Dopita M. A., 2014, ApJ, 781, L12
Richards G. T. et al., 2006, ApJS, 166, 470
Richstone D. et al., 1998, Nature, 395, A14
Rieke G. H., Alonso-Herrero A., Weiner B. J., Pérez-González P. G., Blaylock M., Donley J. L., Marcillac D., 2009, ApJ, 692, 556
Rodríguez-Merino L. H., Chavez M., Bertone E., Buzzoni A., 2005, ApJ, 626, 411
Rola C., Pelat D., 1994, A&A, 287, 676
Rothberg B., Joseph R. D., 2004, AJ, 128, 2098
Rupke D. S. N., Veilleux S., 2011, ApJ, 729, L27
Rupke D. S., Veilleux S., Sanders D. B., 2005, ApJS, 160, 115
Sanders D. B., Soifer B. T., Elias J. H., Madore B. F., Matthews K., Neugebauer G., Scoville N. Z., 1988, ApJ, 325, 74
Schmidt M. et al., 1998, A&A, 329, 495
Schramm M., Silverman J. D., 2013, ApJ, 767, 13
Sell P. H., Pooley D., Zezas A., Heinz S., Homan J., Lewin W. H. G., 2011, ApJ, 735, 26
Sérsic J. L., 1963, Bol. Asoc. Argentina Astron. La Plata Argentina, 6, 41
Shapley A. E., Coil A. L., Ma C.-P., Bundy K., 2005, ApJ, 635, 1006
Shen Y. et al., 2011, ApJS, 194, 45
Smolčić V. et al., 2009, ApJ, 696, 24
Somerville R. S., 2009, MNRAS, 399, 1988
Springel V., Di Matteo T., Hernquist L., 2005, ApJ, 620, L79
Stefanon M., Marchesini D., Rudnick G. H., Brammer G. B., Whitaker K. E., 2013, ApJ, 768, 92
Steinhardt C. L., Elvis M., 2010, MNRAS, 402, 2637
Stern D. et al., 2005, ApJ, 631, 163
Stern D. et al., 2012, ApJ, 753, 30
Strauss M. A. et al., 2002, AJ, 124, 1810
Su M., Finkbeiner D. P., 2012, ApJ, 753, 61
Swade D. A., Hopkins E., Swam M. S., 2001, in Harnden F. R., Jr, Primini F. A., Payne H. E., eds, ASP Conf. Ser. Vol. 238, Astronomical Data Analysis Software and Systems X. Astron. Soc. Pac., San Francisco, p. 295
Thomas D., Maraston C., Bender R., Mendes de Oliveira C., 2005, ApJ, 621, 673
Thomas D., Maraston C., Schawinski K., Sarzi M., Silk J., 2010, MNRAS, 404, 1775
Thompson T. A., Quataert E., Murray N., 2005, ApJ, 630, 167
Tozzi P. et al., 2006, A&A, 451, 457
Trakhtenbrot B., Netzer H., 2012, MNRAS, 427, 3081
Treister E., Urry C. M., Schawinski K., Cardamone C. N., Sanders D. B., 2010, ApJ, 722, L238
Tremonti C. A. et al., 2004, ApJ, 613, 898
Tremonti C. A., Moustakas J., Diamond-Stanic A. M., 2007, ApJ, 663, L77
Trouille L., Barger A. J., Cowie L. L., Yang Y., Mushotzky R. F., 2008, ApJS, 179, 1
Trouille L., Barger A. J., Tremonti C., 2011, ApJ, 742, 46
Trujillo I., Conselice C. J., Bundy K., Cooper M. C., Eisenhardt P., Ellis R. S., 2007, MNRAS, 382, 109
Ulrich M.-H., Maraschi L., Urry C. M., 1997, ARA&A, 35, 445
Urry C. M., Padovani P., 1995, PASP, 107, 803
van de Sande J. et al., 2013, ApJ, 771, 85
van Dokkum P. G. et al., 2008, ApJ, 677, L5
Vanden Berk D. E. et al., 2001, AJ, 122, 549
Veilleux S., Osterbrock D. E., 1987, ApJS, 63, 295
Veilleux S. et al., 2013, ApJ, 776, 27
Verdolini S., Yeh S. C. C., Krumholz M. R., Matzner C. D., Tielens A. G. G. M., 2013, ApJ, 769, 12
Vignali C., Alexander D. M., Gilli R., Pozzi F., 2010, MNRAS, 404, 48
Wagner A. Y., Bicknell G. V., Umemura M., 2012, ApJ, 757, 136
Wagner A. Y., Umemura M., Bicknell G. V., 2013, ApJ, 763, L18
Werner M. W. et al., 2004, ApJS, 154, 1
Wright E. L. et al., 2010, AJ, 140, 1868
Wu J., Brandt W. N., Anderson S. F., Diamond-Stanic A. M., Hall P. B., Plotkin R. M., Schneider D. P., Shemmer O., 2012, ApJ, 747, 10
Wuyts S., Cox T. J., Hayward C. C., Franx M., Hernquist L., Hopkins P. F., Jonsson P., van Dokkum P. G., 2010, ApJ, 722, 1666
Xue Y. Q. et al., 2011, ApJS, 195, 10
Yan R. et al., 2011, ApJ, 728, 38
York D. G. et al., 2000, AJ, 120, 1579
Zabludoff A. I., Zaritsky D., Lin H., Tucker D., Hashimoto Y., Shectman S. A., Oemler A., Kirshner R. P., 1996, ApJ, 466, 104
Zirm A. W. et al., 2007, ApJ, 656, 66
Zubovas K., King A. R., 2014, MNRAS, 439, 400
Zubovas K., Nayakshin S., King A., Wilkinson M., 2013, MNRAS, 433, 3079

APPENDIX A

A1 Creation of the PSFs for GALFIT

From the multidrizzled images, we created high S/N, representative PSFs for each galaxy, critical for performing 2D galaxy fitting of our ultracompact galaxies (Fig. A3). We used a strategy similar to that of Canalizo et al. (2007) to create our PSFs and come to similar conclusions regarding PSF selection. Since we did not have separate stellar PSF images, we hand-selected single, isolated stars by-eye that were not too faint (>1000 peak counts) or saturated ($\lesssim$60 000 peak counts). We verified that each star was indeed an unsaturated

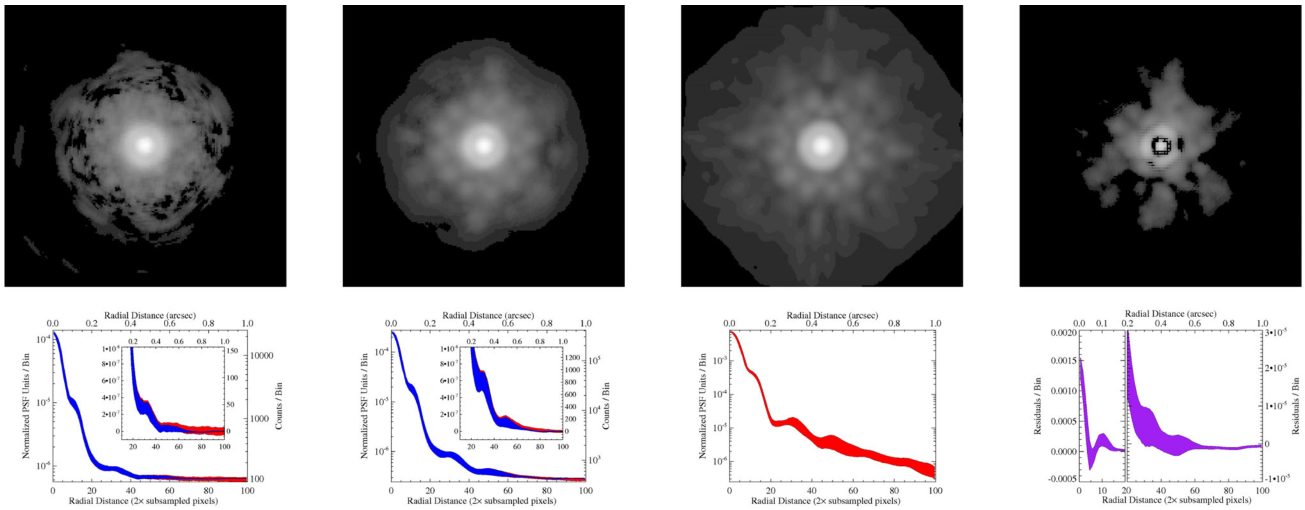

Figure A1. First row (images from left to right): J0826+43, lowest S/N stacked PSF; J2118+00, highest S/N stacked PSF; TinyTim ('tiny2' stage) PSF convolved with a Gaussian to try to match J2118+00's PSF in GALFIT; residuals between previous two PSFs. The images have been considerably stretched to show all parts of the PSF out to the faint wings. The scales in all images have been matched to each other. All images are 2 arcsec × 2 arcsec. Second row: the radial profiles corresponding to each respective image. For the first two plots from the left, the larger plot contains the stacked PSF profile that has not been background subtracted and the inset contains the background-subtracted profile, focusing on the faint end of the PSF at large radii. The inset axes have the same units as their larger counterparts, except that each right y-axis is the background-subtracted counts. The third plot from the left is the radial profile of the model PSF, which was not smoothed. The fourth plot from the left is the radial profile of the GALFIT residuals for when we convolved the TinyTim ('tiny2') PSF with a Gaussian to try to match J2118+00's PSF. The width of all profiles represents the standard deviation of the pixel values at each radial bin. The red and blue colours are the unsmoothed and smoothed PSFs, respectively.

point source by plotting its radial profile and calculating its FWHM. We identified 4–36 PSF stars per image, which depended on the stellar density of the observed field.

For each star, we extracted 2 arcsec × 2 arcsec stamps approximately centred on each star, subsampled each stamp by a factor of 10 in each dimension, and centroided each star in its stamp. Using these stars, we calculated a single stacked PSF for each galaxy, weighting the stars by their integrated counts. We sampled the resulting PSF back up by a factor of 5 so that it was two times oversampled. Then, we smoothed the outermost sections of each stacked PSF using a median-filtered box that increases in radius starting 0.2 arcsec away from the centre of the stacked PSF.[10] Finally, we background subtracted and normalized the PSF so that it could be used for the galaxy fitting.

Some PSFs are better determined than others because of the presence or lack of bright stars in each image and the positions of those bright stars relative to the galaxy. This results in differences in S/N between the PSFs, which does not appear to significantly bias our galaxy fits. We show our highest and lowest S/N PSFs in Fig. A1. The J2118+00 PSF has the most background-subtracted counts ($\gtrsim$11 million) while the J0826+43 PSF is comprised of the fewest background-subtracted counts ($\sim$700 000). While it is tempting to substitute the PSF from J2118+00 for the PSF from J0826+43, we chose not to do this for a number of reasons: the focus clearly changes significantly from image to image, the orientation of the PSF clearly changes through the rotation of the slightly asymmetric airy pattern, etc. We conclude that the uncertainty introduced from using a PSF from a different image (e.g. having to rotate it) is probably at least as large as the uncertainty from using the lower S/N PSF.

We also attempted to make use of the *HST* PSF modelling tool, TinyTim (Hook & Stoehr 2008), as it provides infinite S/N. Because the final step in creating the TinyTim PSF (the 'tiny3' stage) currently does not resample and distort the PSF in the same way as multidrizzle, we fit this PSF in GALFIT with our highest S/N stacked image PSF (from J2118+00) using a Gaussian (to broaden the PSF to match the image better). Note that the TinyTim PSF was first rotated to the nearest degree to match the orientation of the stacked PSF image so that χ^2 was minimized. This matched the roll orientation of the telescope to within a few degrees, as expected.

The output model (convolved) PSF and the residuals from the fit are shown in Fig. A1. The focus offset for the creation of the model PSF with TinyTim was not well determined as the model and measured focus differed considerably.[11] However, tests indicated that χ^2 returned by GALFIT changed negligibly for various reasonable focus offsets (within ±0.4 μm). We conclude that determining the correct rotation is important for creating a PSF with TinyTim, but that the difference in focus offsets for reasonable focus values is negligible.

As is evident in Fig. A1, the TinyTim PSF does not match the image PSF very well. The largest source of uncertainty in the TinyTim PSF model as noted by the *HST* team[12] appears to be the aberration coefficients used to generate the PSF, which are not well modelled for WFC3. Because of these many complications and the fact that the *HST* team recommends the use of empirical PSFs, we chose not to use the convolved TinyTim PSF in our analysis. For each galaxy, we used the stacked stellar PSF from the respective image only.

A2 2D image fitting parameter uncertainties

The statistical uncertainties provided by GALFIT are not very meaningful because the rigorous meaning of χ^2 is violated to a large extent during fitting.[13] The errors reported by GALFIT underestimate

[10] halo_smooth.pro, http://132.248.1.102/~morisset/idl/pro/starfinder/

[11] http://www.stsci.edu/hst/observatory/focus/FocusModel
[12] http://www.stsci.edu/hst/observatory/focus/TinyTim
[13] http://users.obs.carnegiescience.edu/peng/work/galfit/CHI2.html

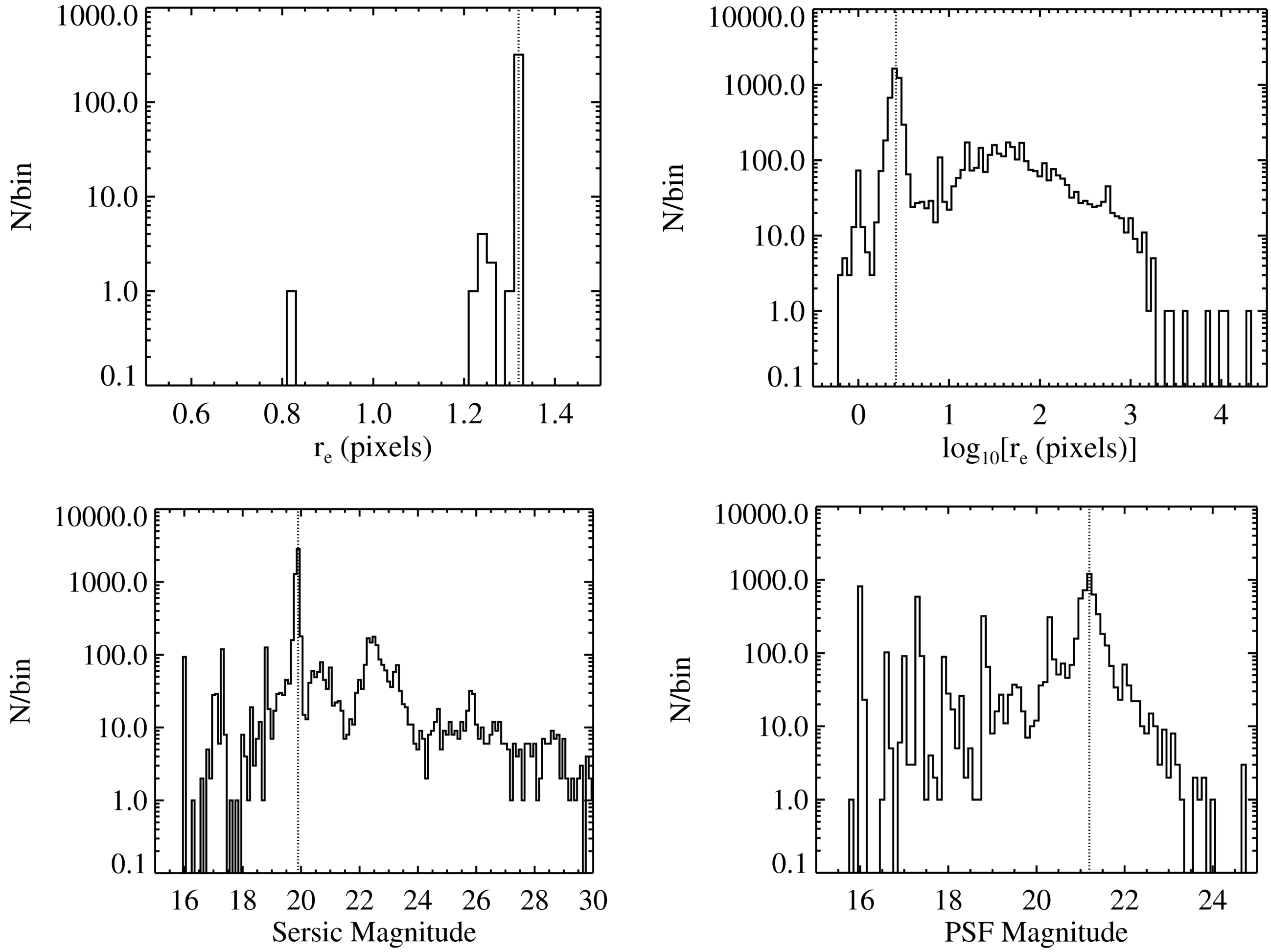

Figure A2. The results of multiple GALFIT runs with different starting parameters for J1713+28. We chose this galaxy as a worst-case example because it has two cores that are each fitted with a Sérsic + PSF model, and, therefore, has the largest number of free parameters. The first plot is for the Sérsic only fit to this galaxy, and the remaining plots are for the Sérsic + PSF model. The distribution of the Sérsic magnitudes for the Sérsic-only model is singly and very tightly peaked like r_e. All plots are for the primary core. The vertical dotted lines are at the best-fitting values.

the true error. However, it is important to quantify degeneracies in the model fits so that we can quantitatively ascertain how meaningful the fits are, especially when we add a PSF to the model.

To explore the robustness of our derived model parameters, we began the fits from fixed grids of a range of parameter starting values. This also verifies that GALFIT has found the global minimum and that the fit is not sensitive to starting parameter values, which we found could be true for the more complicated models (e.g. J1713+28: a Sérsic and PSF for each core). For each model fit, we created a grid of hundreds to thousands of starting parameter combinations (depending on the number of free parameters) and normally ran GALFIT until it found a minimum or crashed. We show some example distributions for J1713+28 in Fig. A2.

This approach enables us to roughly quantify the degeneracies in our model parameters. The distributions in the parameter values are always at least as large as the statistical uncertainties returned by GALFIT. This approach is particularly useful because it highlights the expected considerable increase in uncertainty of the parameter values as more complicated models are introduced (more degeneracies between model parameters). For instance, note that, while the effective radius is well determined for a single Sérsic fit per core, the uncertainty is almost always much larger when a PSF model is included. In this case, for almost every galaxy, the addition of the PSF assumes a large fraction of the core light, leading the Sérsic to fit more extended diffuse emission. However, because the underlying emission is so much fainter than the core, its extent is not as well determined as the extent of the predominant core emission in a Sérsic-only model. For instance, the spread in the effective radii and Sérsic magnitudes is ∼10–100 times larger when both the PSF and the Sérsic model are simultaneously fitted versus fitting only a single Sérsic model. This suggests that, while adding a PSF to the model to better understand how PSF-like the galaxies are, the best-fitting parameters should be interpreted with caution.

A3 Additional images and radial profiles

We provide radial profiles and cutouts of the fitting region and masked residuals images in Fig. A3. Details of the masking and fitting process are discussed in Section 3.2.1.

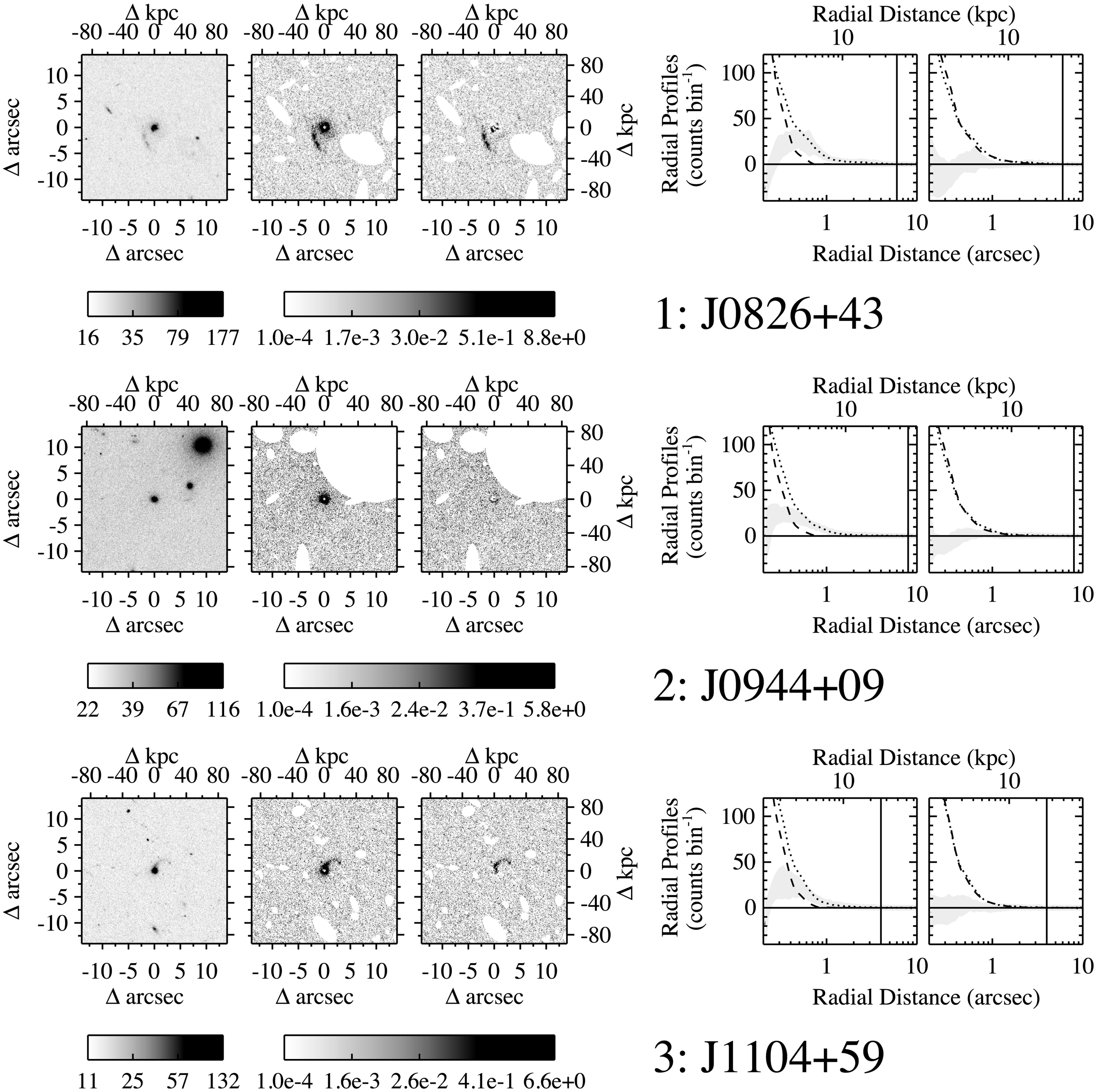

Figure A3. From left to right for each of our 12 galaxies: the 1400 pixel × 1400 pixel cutout from the original image that we fit with GALFIT; the residual image from the Sérsic model fit; the residual image from the Sérsic + PSF model fit; radial profiles of the galaxy, best-fitting model, and residuals for the Sérsic and Sérsic + PSF fits. The three images are logarithmically scaled using the sky level and the Sérsic magnitude to define the stretch; the colour bars are in units of *HST* counts per pixel. Regions that are masked during the fit are shown as white in the residual images. North is up and east is left. We plot the radial profiles for the masked, sky-subtracted original image (dotted), the masked, sky-subtracted model (dashed), and the masked residual image (shaded; the width corresponds to the standard deviation of the pixel values in each radial bin). We do not show the innermost region of the radial profile ($r < 10$ pixels) because these regions are dominated by noise from the imperfect PSFs. If the inner radius of the sky region is within 10 arcsec, it is denoted by a solid vertical line. Note that J1506+61 and J1713+28 are always fitted with two $n = 4$ Sérsic models as they have two clearly distinct, associated, bright cores. When a PSF is also applied to J1506+61, only one PSF is used because the fit to the fainter core does not favour a PSF, whereas, two PSFs are used for J1713+28, one per core.

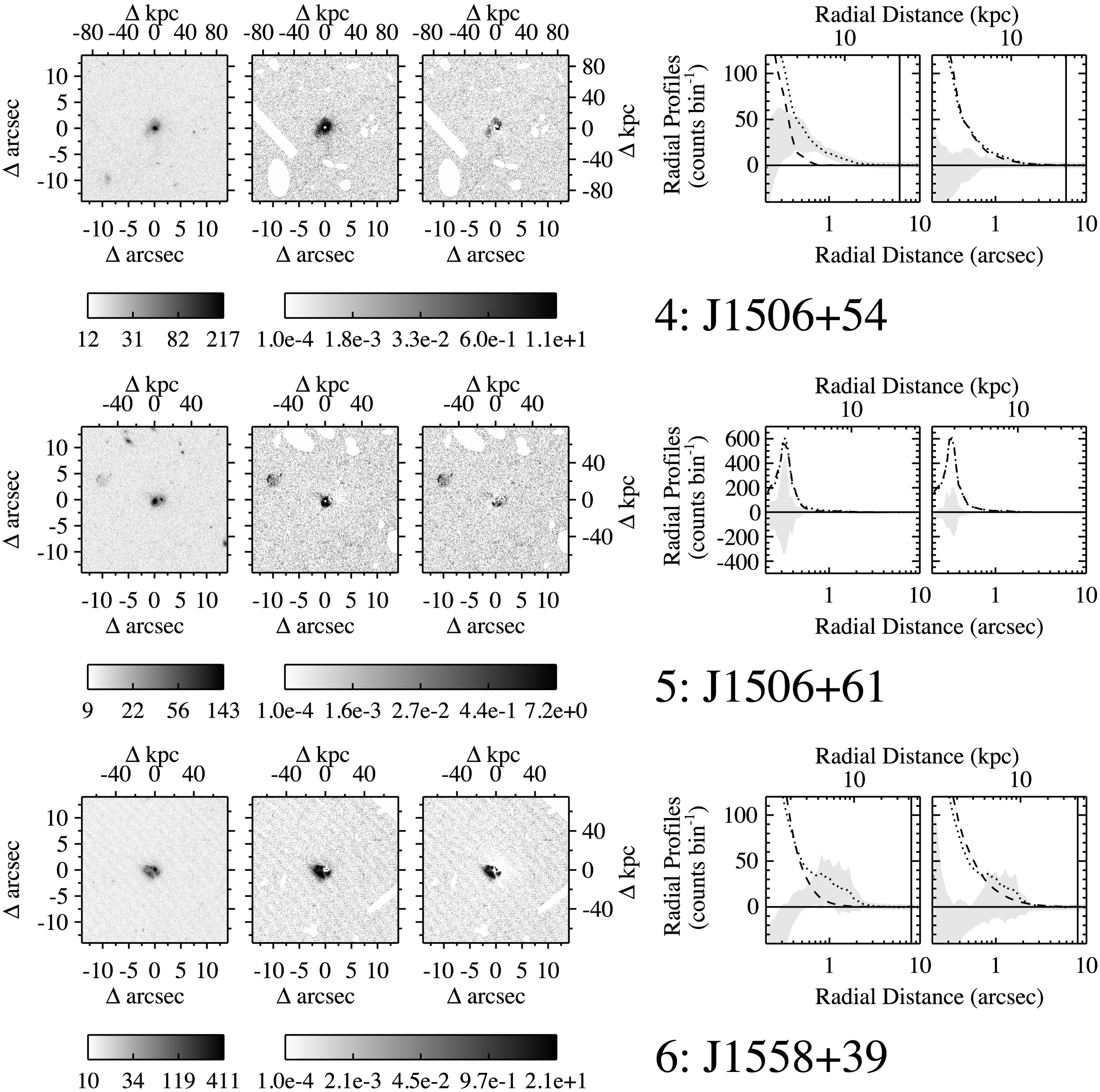

Figure A3 – *continued*

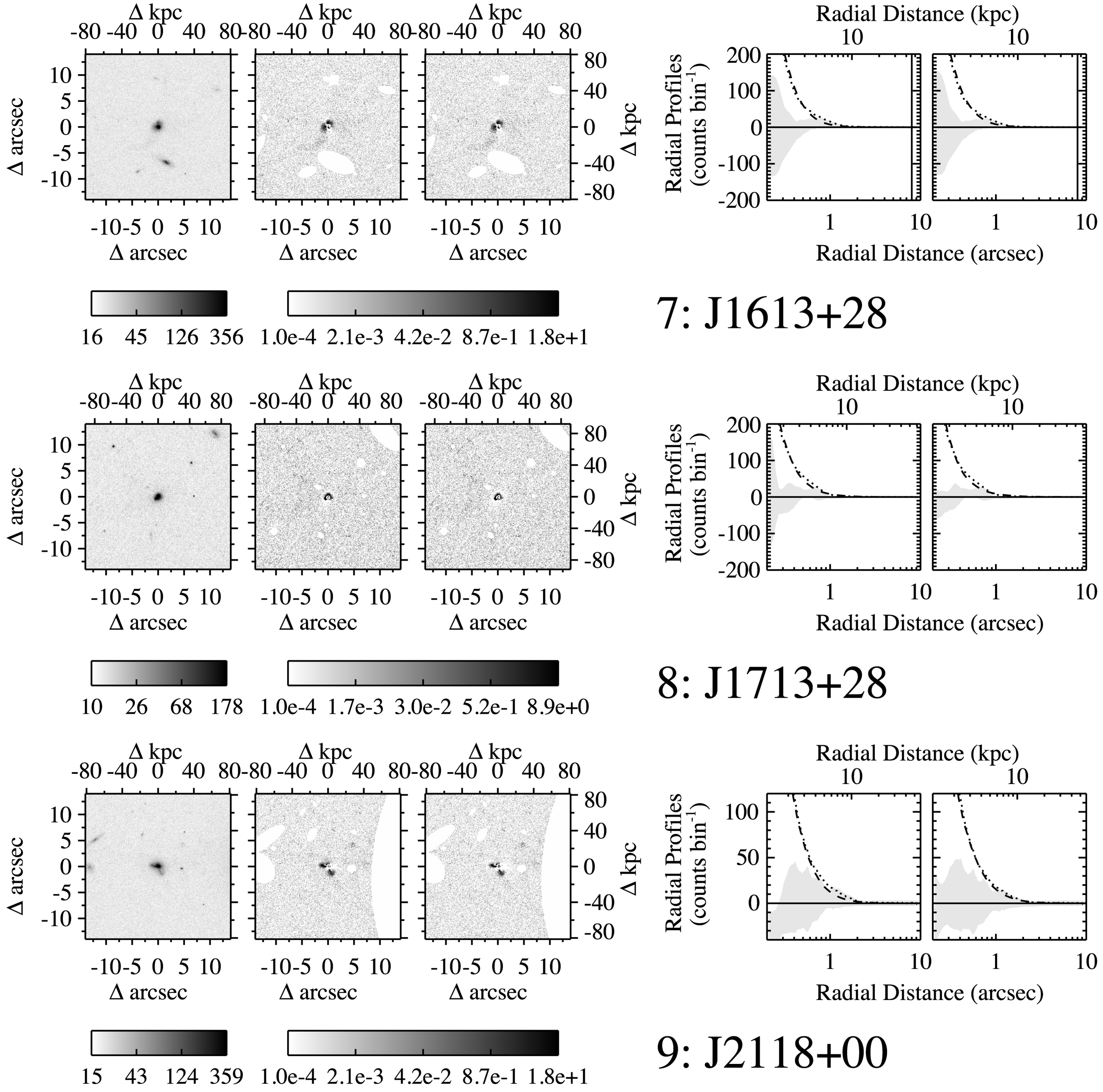

Figure A3 – *continued*

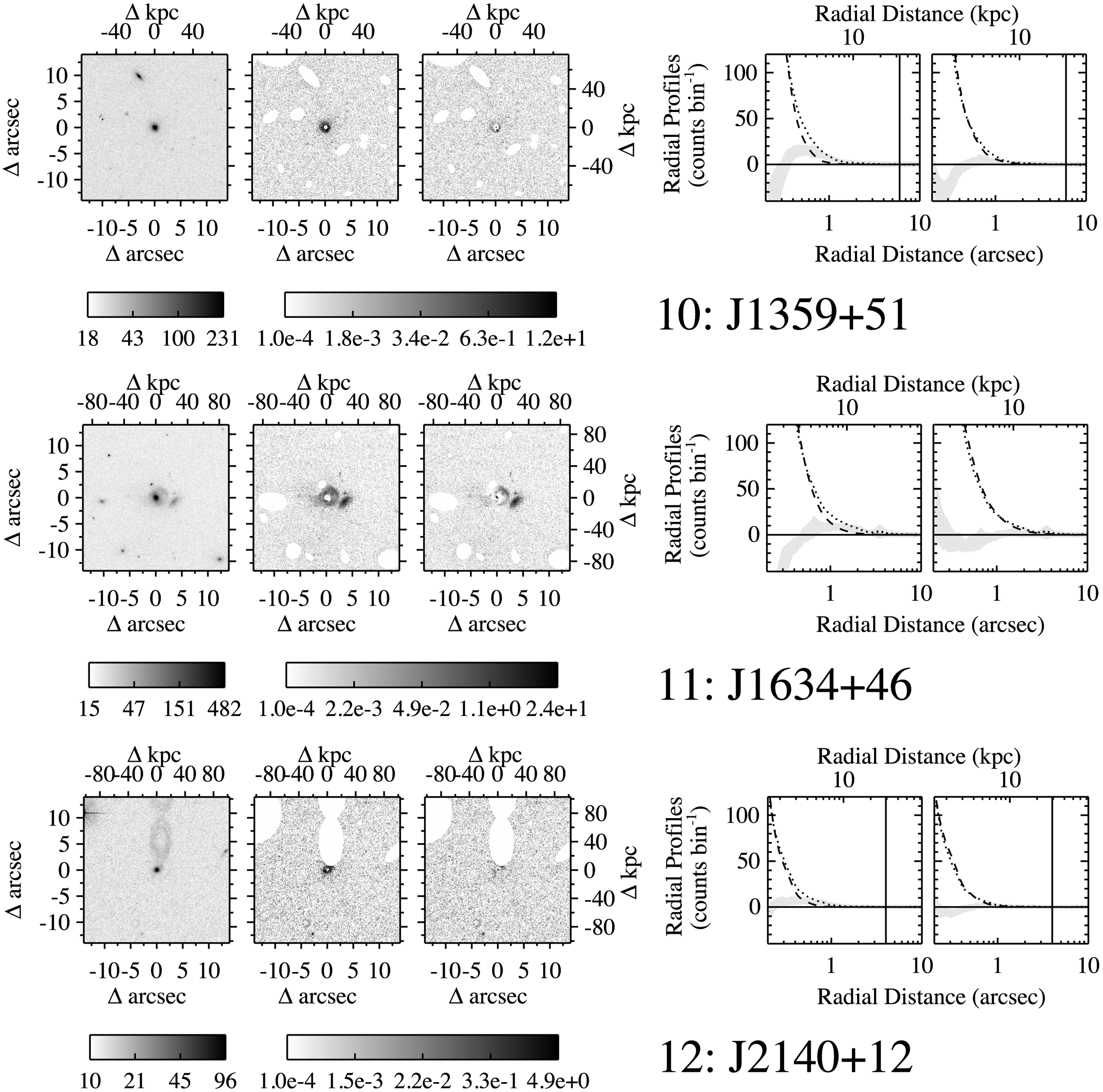

Figure A3 – *continued*

This paper has been typeset from a TEX/LATEX file prepared by the author.